Ocean Engineering 293 (2024) 116618

Contents lists available at ScienceDirect

Ocean Engineering

journal homepage: www.elsevier.com/locate/oceaneng

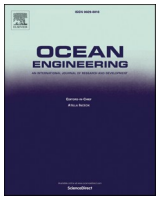

Research paper

Hydrodynamic analysis of a heave-hinge wave energy converter combined with a floating breakwater

Yujia Wei [a], Shuangrui Yu [b], Xiang Li [b], Chongwei Zhang [c,**], Dezhi Ning [c], Luofeng Huang [a,*]

[a] School of Water, Energy and Environment, Cranfield University, Cranfield, MK43 0AL, UK
[b] Department of Naval Architecture, Ocean and Marine Engineering, University of Strathclyde, Glasgow, G4 0LZ, UK
[c] State Key Laboratory of Coastal and Offshore Engineering, Dalian University of Technology, Dalian, 116024, China

ARTICLE INFO

Handling Editor: Prof. A.I. Incecik

Keywords:
Floating breakwater
Wave energy converter
Fluid-structure interaction
Hydrodynamics
Multi-body dynamics
OpenFOAM

ABSTRACT

Research interest in breakwater design has increased recently due to the impetus to develop marine renewable energy systems, as breakwaters can be retrofitted to harness wave energy at the same time as attenuating it. This study investigates a novel system of attaching a hinge baffle under a floating breakwater. The floating breakwater itself acts as a heaving wave energy converter, and meanwhile the hinge rotation provides a second mechanism for wave energy harnessing. A computational model with multi-body dynamics was established to study this system, and a series of simulations were conducted in various wave conditions. Both wave attenuation performance and energy conversion ratio were studied, using an interdisciplinary approach considering both coastal engineering and renewable energy. In particular, the performance of the proposed system is compared with contemporary floating breakwater designs to demonstrate its advantage. Overall, a useful simulation framework with multi-body dynamics is presented and the simulation results provide valuable insights into the design of combined wave energy and breakwater systems.

1. Introduction

Along with the increase of coastal and offshore projects, traditional bottom-mounted breakwaters are less used than floating breakwaters that use less material, induce smaller environmental impacts and can operate regardless of the water depth and seabed conditions (Huang and Li, 2022a; Dai et al., 2018; Chen et al., 2023; Zhou et al., 2022). Floating breakwaters, originally designed to attenuate waves, are nowadays considered to have an additional function of Wave Energy Converter (WEC), as the dissipated wave energy can be directly converted to electricity (Cheng et al., 2022a; Zhang et al., 2020a, 2020b; Khojasteh et al., 2023). In addition, floating breakwaters can be integrated into the edge of other offshore renewable energy systems (e.g. floating solar farms) to protect them from wave attacks (Wei et al., 2023).

The design of floating breakwaters has been extensively studied over the past few decades due to its scientific and practical significance (Dai et al., 2018; Adee, 1976). Given the variety of WEC systems (Dai et al., 2018), there are numerous possible combinations for WEC-breakwater systems, such as Oscillating Body (OB)-breakwater (Guo et al., 2021; Zhang et al., 2020c), and Oscillating Water Column (OWC)-breakwater (Luo et al., 2014; Elhanafi et al., 2017; He et al., 2014). Among these, the OB-breakwater are particularly appealing for forming a hybrid system. They offer dual functions of coastal protection and wave energy utilisation due to their durability, simplicity and ease of construction (Zhao et al., 2019). Some floating box-type breakwaters have even reached the stage of engineering applications (Dai et al., 2018; Maritime, 2005).

The OB-type WEC adopts a movable body to serve as an "absorber" to capture wave energy, which is connected to a Power Take-Off (PTO) system to convert the kinetic energy of the body into electricity; the PTO adds mechanical damping to the movable body (Bozzi et al., 2013; Xu et al., 2019). The wave attenuation performance and energy conversion efficiency of such a hybrid WEC-breakwater system have been studied using a range of research methods, including analytical methods (Zhao et al., 2017, 2021; Diamantoulaki et al., 2008; Koutandos et al., 2004), experimental tests (Ning et al., 2016; Zhao et al., 2018), and computational simulations (Zhang et al., 2020a; Ram et al., 2022).

Previous research has provided significant insights into the design concepts of the integrated OB-breakwater, including design aspects (Zhang et al., 2020a), mooring dynamics (Vicente et al., 2013; Tagliafierro et al., 2022) and their hybrid applications (Zhao et al., 2019;

* Corresponding author.
** Corresponding author.
E-mail addresses: chongweizhang@dlut.edu.cn (C. Zhang), Luofeng.huang@cranfield.ac.uk (L. Huang).

https://doi.org/10.1016/j.oceaneng.2023.116618
Received 8 September 2023; Received in revised form 8 December 2023; Accepted 18 December 2023
Available online 2 January 2024

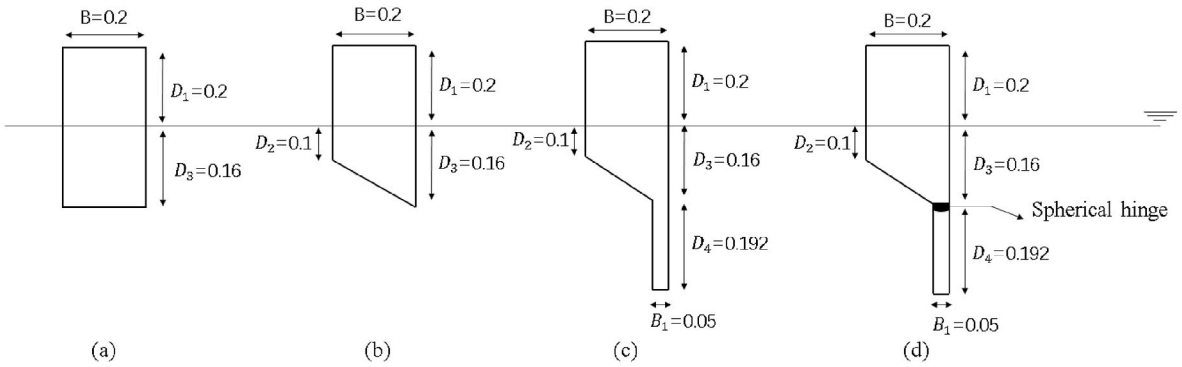

Fig. 1. Schematic diagram of hybrid WEC & floating breakwater devices with different geometries, (a) square bottom, (b) wedge bottom, (c) Triangular baffle bottom (d) Hinged baffle bottom.

Cheng et al., 2022b, 2022c; Ning et al., 2017). It was demonstrated that the geometric shape of such a combination significantly impacts on system characteristics and performance. Zhang et al. (2020a) used computational simulations to report that symmetric shapes of WECs have lower energy conversion efficiency than asymmetrical ones, as the latter can reduce the waste of wave energy induced by fluid viscosity. Compared with a symmetric square box shape, the authors demonstrated that an asymmetrical wedge shape can harness more wave energy as well as enhance wave attenuation. In line with this, one benchmark design "the Berkley wedge" (Madhi et al., 2014) was proposed and experimental tests showed agreement with Zhang et al. (2020a). Reabroy et al. (2019) proposed a dolphin and trapezoid shape of WEC integrated with a fixed breakwater, and they analyzed the effect of the slenderness and sharpness of the WEC geometry on its performance. In their design, the feature edges of the floater were rounded to avoid the local vorticity, resulting in a reduction of wave dissipation so as to increase the amount of wave energy that the WEC can absorb. Zhang et al. (2020b) conducted further simulations of a dual-WEC system. They placed two OBs in computational simulations with a small gap in between, which demonstrated an improvement in both better wave attenuation and wave energy extraction than operating two OBs in isolation, which is attributed to the resonance behaviour in the gap.

Although it has become a consensus that asymmetrical shapes can offer better wave attenuation and energy harnessing than symmetrical ones, and an essential factor to enhance both aspects is to reduce fluid vorticity, the geometry can still benefit from further improvement. The geometrical shapes studied in previous research are illustrated in Fig. 1, ranging from the simple square bottom shape (Fig. 1(a)), wedge bottom shape (Fig. 1(b)), triangular baffle bottom (Fig. 1(c)), which is depicted following Zhang et al. (2020a). It can be deduced that the triangular baffle bottom (Fig. 1(c)) could remain significant vortices, despite that it may be better than the previous two designs. Meanwhile, the thin baffle at the floater's bottom may introduce higher stress concentrations in practical and local bending moments as it moves upside down during periodical wave motions. To address this, this study introduces a new geometry – a hinged baffle design as given in Fig. 1 (d), where the hinge motion may effectively mitigate fluid vortices and stress concentration.

Additionally, the hinge may serve as another rotating PTO, which helps further harness wave energy. This concept is inspired by other WEC concepts, such as the pitching-wall WEC device (Benites-Munoz et al., 2020). Guo et al. (2021) showed that the interaction between the pitch motion of a front wall significantly broadens the frequency bandwidth of energy conversion efficiency in comparison with the traditional OWC device with a fixed front wall. Yu et al. (2016) proposed a WEC consisting of two rafts and one pendulum hung at the joint of the rafts. By installing the hinge-baffle "pendulum", the capture width ratio of the WEC was evidently increased, similar to Guo et al. (2021). Yu et al. (2023) further proposed an active damping control method to adjust the spring stiffness for a pitching wall according to the wave condition, which maximises the PTO's power. However, the authors inferred that the capture width ratio of WEC may be overestimated by using the inviscid flow theory. They recommended using higher-order methods for the further investigation of such WEC systems.

Based on the above literature scan, the performance of the heave-hinge WEC-breakwater system (Fig. 1(d)) is evaluated in this paper based on a high-fidelity computational simulation approach. In the computational approach, the Navier-Stokes equations were used to simulate unsteady wave flows, which are coupled with Multi-Body

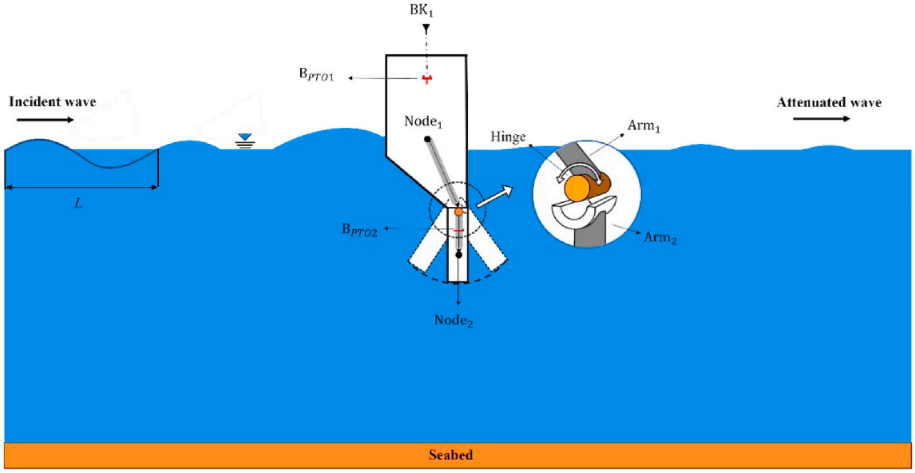

Fig. 2. Illustration of the HH WEC-breakwater system.

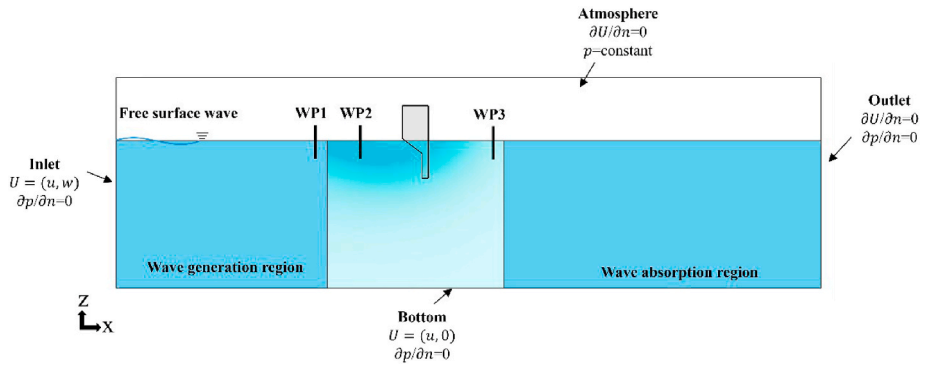

Fig. 3. Schematic of wave domain and pressure gauges.

Dynamics (MBDs) of structures to simulate the heave-hinge bodies. The fluid and structural parts are coupled in a fully two-way manner. The primary variables studied include wave attenuation and energy conversion efficiency, which are compared with contemporary designs introduced in previous work (Fig. 1(a–c)).

This paper is organised as follows: Section 2 introduces the mechanical principles of the heave-hinge WEC-breakwater system and introduces its simulation methodology. Section 3 presents the verification and validation of the model. Section 4 presents systematic simulations and discusses the results. Finally, concluding remarks are drawn in Section 5.

2. Methodology

2.1. Heave-hinge wave energy converter

The Heave-Hinge (HH) WEC, shown in Fig. 2, combines the functionalities of wave attenuation and wave energy conversion. The system utilises an axisymmetrical floater design equipped with a heave PTO damping, B_{PTO1}. The bottom of the floater is attached with a hinge baffle, featuring another rotational PTO damping, B_{PTO2}. Two linking arms (Arm_1 *and* Arm_2) are connected between the mass centres of these two components ($Node_1$ *and* $Node_2$) to transfer forces and moments for restraints.

2.2. Computational domain

To simulate the HH WEC-breakwater system, a two-dimensional Numerical Wave Tank (NWT) is established, as illustrated in Fig. 3. The NWT has a length of L_x in the x direction, which is taken to be 5.5 times the wavelength λ, with 2.5 λ places in front of the breakwater and 3 λ behind it. The height in the z direction L_z is set to be 1.3 times the water depth h. The centre of the Cartesian coordinate system coincides with the centre of mass of the breakwater's original position. The density of water is 10^3 kg/ m^3 and the density of air is 1 kg / m^3. Dynamic viscosity values of $1e^{-6}m^2/s$ and $1.48e^{-5}m^2/s$ are used for water and air, respectively. Three wave gauges (WP_1–WP_3) are placed within the wave domain. WP_1 and WP_2 are placed in front of the breakwater, with horizontal locations of -2.4 m and -1.6 m, respectively. WP_3 is placed at the rear side of the breakwater, with a horizontal location of $+0.8$m to capture the dissipated wave elevation in the temporal domain.

The presented NWT had the following boundary conditions: at the inlet boundary, the fluid velocity was prescribed to generate regular waves. The static pressure condition was used on the domain top to mimic the atmosphere. The domain bottom was set as a wall type to model the seabed. No-slip boundary conditions were assigned to the structure surface. At the outlet boundary, the zero-gradient condition was adopted.

2.3. Fluid solver

The simulation of fluid flow is performed using the open-source Computational Fluid Dynamics (CFD) code OpenFOAM, specifically, the multi-phase solver "interFoam" (Huang et al., 2022b). The flow is modelled as unsteady, incompressible and viscous, governed by the continuity and momentum equations as given below:

$$\nabla \cdot U = 0 \tag{1}$$

$$\frac{\partial \rho U}{\partial t} + \nabla \cdot \left(\rho\left(U - U_g\right)\right) = -\nabla P_d - g \bullet x \nabla \rho + \nabla\left(\mu_{eff} \nabla \mathrm{U}\right) + (\nabla \mathrm{U}) \bullet \mu_{eff} + f_\sigma \tag{2}$$

where U is the velocity of the flow field, ρ denotes the mixed density of water and air, g is the gravity acceleration, P_d represents the dynamic pressure, μ_{eff} is the effective dynamic viscosity, f_σ is the surface tension which is only considered at the free surface.

The Volume of Fluid (VOF) method (Hirt et al., 1981) is adopted to simulate the free surface in the numerical domain by solving an additional transport equation for the scalar quantity, a, which represents the volume fraction of fluid for each cell.

$$\frac{\partial a}{\partial t} + \nabla \bullet \left[\left(U - U_g\right) a\right] + \nabla \bullet \left[U_r (1 - a) a\right] = 0 \tag{3}$$

where U_r is the artificial compressive velocity which only functions near the free surface due to the inclusion of $(1 - a)a$.

For a two-phase flow problem, the volume fraction of each phase is used as the weighting factor to calculate the mixture properties. The equations for the density and the viscosity can be expressed by:

$$\rho = a\rho_w + (1 - a)\rho_a \tag{4}$$

$$\mu = a\mu_w + (1 - a)\mu_a \tag{5}$$

where subscripts w and a represent the water and air phases, respectively.

In this study, the Stokes second-order waves are generated and absorbed in the numerical wave tank (NWT) using "waves2Foam" toolbox (Jacobsen et al., 2012). The relaxation zone technique is adopted to improve wave quality near the inlet boundary (λ) and remove undesired reflection at the outlet boundary (1.5λ). The following equations specify the primary function of the relaxation zones:

$$a_R(\chi_R) = 1 - \frac{\exp\left(\chi_R^{3.5}\right) - 1}{\exp(1) - 1} \tag{6}$$

$$\varphi_R = \omega_R \varphi_R^{computed} + (1 - \omega_R)\, \varphi_R^{target} \tag{7}$$

where φ_R refers to either the velocity or volume fraction of water a. The

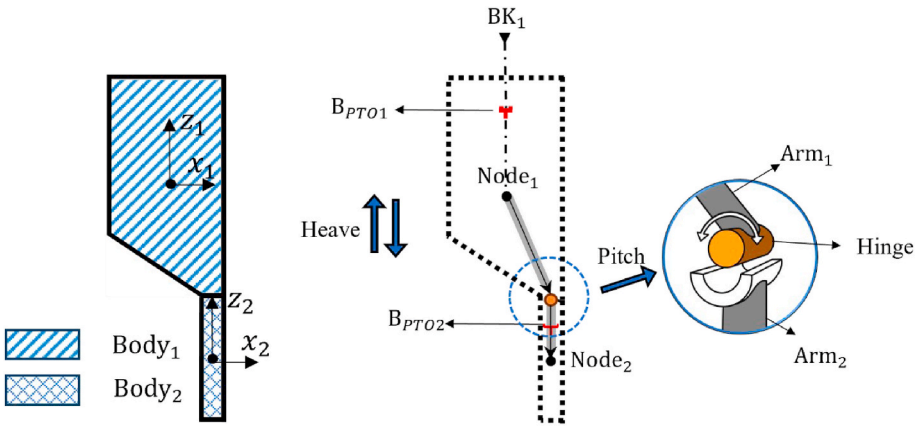

Fig. 4. Two-body hinged modelling in MBDyn and demonstration.

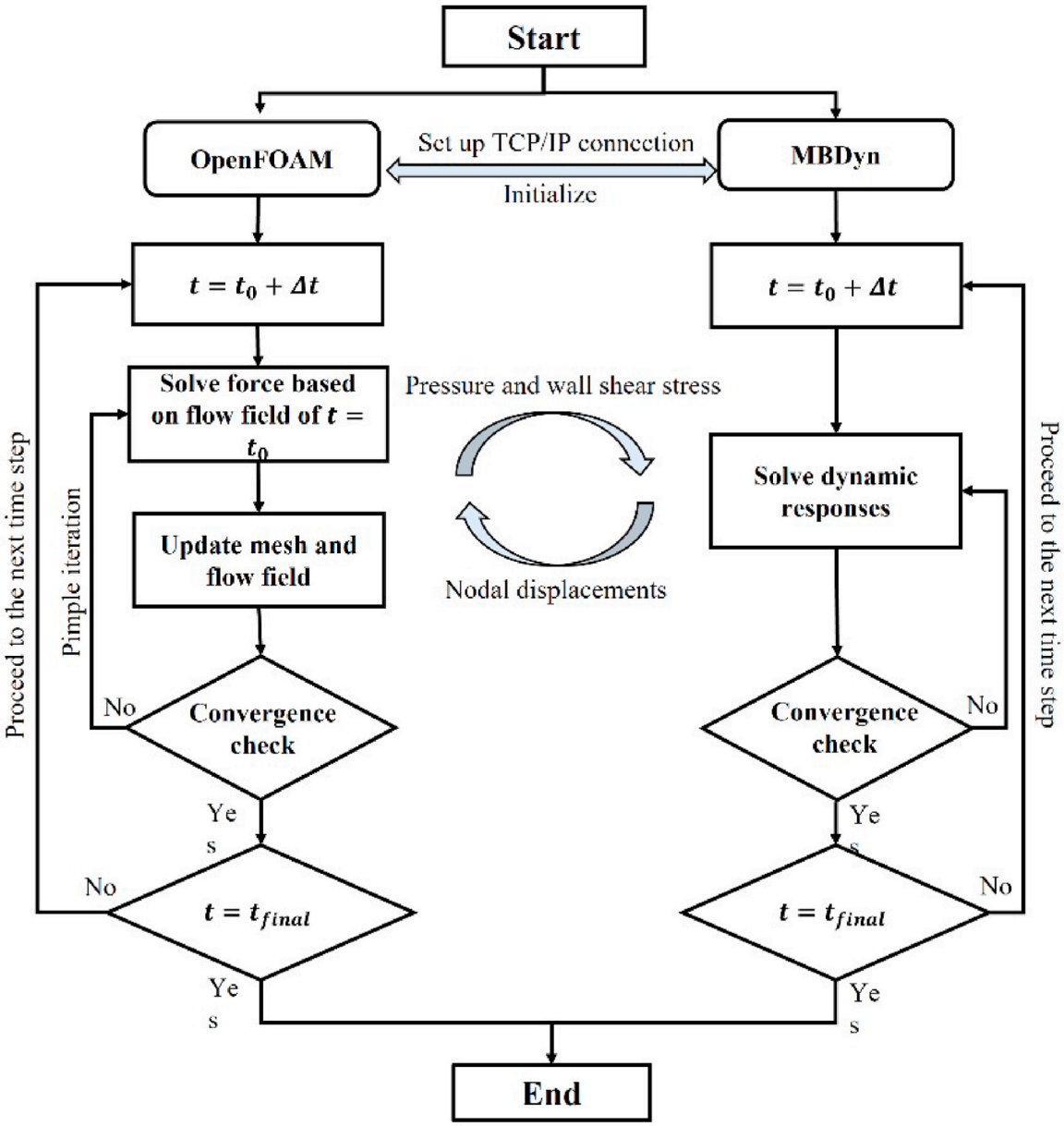

Fig. 5. The workflow of the two-way coupled CFD-MBD approach.

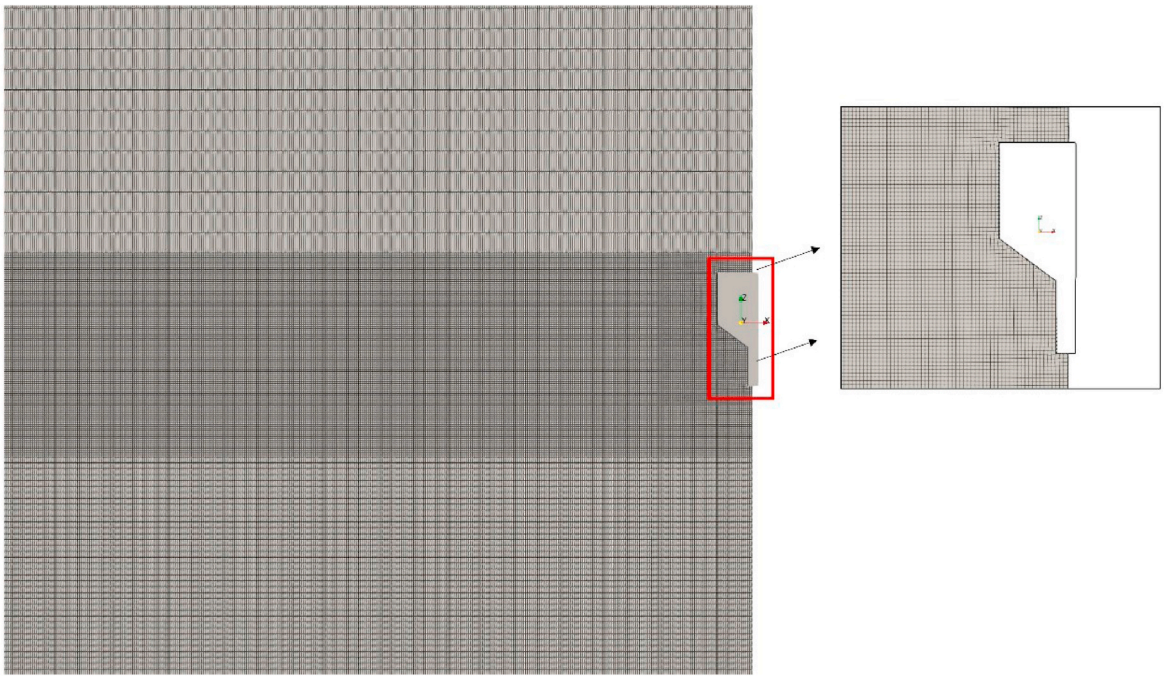

Fig. 6. Mesh structure and refinements of the present model.

weighting function a_R is always equal to 1 at the interface between the non-relaxed computational domain and the relaxation zones, and χ_R is a value between 0 and 1.

The free surface wave was generated according to the theory of Méhauté and Media (1976). Regular waves were generated in medium-deep water conditions with wave steepness less than 0.05 throughout this work, and Stokes's second-order wave equations were used to prescribe the incident waves:

$$\eta = \frac{H}{2}\cos(\theta) + k\frac{H^2}{4}\frac{3-\sigma^2}{4\sigma^3}\cos(2\theta) \tag{8}$$

$$u = \frac{H}{2}\omega\frac{\cosh(kz)}{\sinh(kz)}\cos(\theta) + \frac{3}{4}\frac{H^2\omega k cosh(2kz)}{4\,sinh^4(kh)}\cos(2\theta) \tag{9}$$

$$w = \frac{H}{2}\omega\frac{\sinh(kz)}{\sinh(kz)}\sin(\theta) + \frac{3}{4}\frac{H^2\omega k sinh(2kz)}{4\,sinh^4(kh)}\sin(2\theta) \tag{10}$$

where H is the wave height, wave propagation angle $\theta = kx - \omega t + \psi$ with k being the wave number, ω is the angular wave frequency, and ψ is the wave phase and $\sigma = \tanh(kh)$.

2.4. Structural solver

The multi-body solver MBDyn is employed for structure modelling, which uses Lagrange multipliers or redundant coordinate set formations for multibody systems. The two-body hinged system consists of two separate rigid bodies ($Body_1$ and $Body_2$), connecting by a spherical hinge with an offset between $Node_1$ and $Node_2$, as shown in Fig. 4. Physical properties, such as mass m, and moment of inertia I are saved in the body element and attached to the corresponding structure node (Node). These Nodes denote the rigid bodies with six degrees of freedom (position and orientation), describing the kinematics of rigid-body motion in space.

Two damping systems B_{PTO1} and B_{PTO2} are applied in this study. The first damping system consists of a pair of deformable displacement joints between the fixed background node BK_1 and $Node_1$, providing the heave damping coefficient. The second system, B_{PTO2} uses a deformable hinge element between the hinge point and $Node_2$ to achieve rotation damping. Arms are used between the node and hinge to support the transfer of force and moment. Additionally, a pair of total joint elements is applied to the hinged-baffle's rotation only in the pitch direction. As a result, the two-body hinged system enables a coupled motion, including the global heave response of both the floater and the baffle, and the baffle can self-spin. The dynamic response of the HH WEC-breakwater system is analytically derived, as presented in Appendix A.

2.5. Fluid-structure interactions

In order to estimate the hinged-body responses in waves, a partitioned FSI approach is applied in this study, which coupled OpenFOAM and MBDyn using a two-way weak algorithm. Fig. 5 shows the workflow of the present CFD-MBD approach, where two solvers communicate through sockets. The OpenFOAM solver acts as the main solver, while MBDyn acts as the slave solver. More detailed descriptions of the communication procedure and algorithm can be found in (Wei et al., 2022).

Within the FSI framework, fluid and structural data communication was performed inside each iteration to stabilize the simulation and preserve equilibrium conditions on the interface. The CFD solver calculates scalar quantities of pressure and wall shear stress on patch surfaces, which are then transferred to the corresponding structure nodes in MBDyn. By accepting the force data, MBDyn predicts the rigid body responses and feeds the motion information back to the CFD solver. The fluid mesh is updated simultaneously based on the dynamic mesh technique of mesh motion, which relies on the solution of Laplace transport equations for the displacement point fields.

2.6. Discritisation of the computational domain

A Finite Volume Mesh (FVM) is generated in order to solve the Navier-Stokes equations (Jasak et al., 2007). The domain mesh is created using the uniform hexahedra cells, with the structural geometry (the WEC-breakwater) being carved out Dynamic mesh is applied to fit the motion of the geometry during the simulation. The mesh quality is constantly checked whilst a simulation is running, ensuring the skewness face angle remains under 4°, and the non-orthogonal face is under

30°. Otherwise, a re-meshing step is automatically performed to fit the transient structural status. The grid density at the free surface for multi-phase flow studies is refined to obtain highly accurate results of the wave surface, which makes sure that at least 12 cells per wave height are used on the free surface modelling, which fulfils the guideline from ITTC (ITTC and ITTC Quality System Manual Recommended Procedures and Guidelines, 2017). Fig. 6 shows the generated mesh and its refinements.

2.7. Performance evaluation parameters

- Energy conversion efficiency η_e.

The energy conversion efficiency η_e is an important indicator for evaluating the hydrodynamic efficiency of WECs, which can be expressed as:

$$\eta_e = E_p / E_w \tag{11}$$

where, E_p denotes as the average wave energy conversion power, is the summation of $E_p = E_{p1} + E_{p2}$; E_{p1} is the power generated from the upper point absorber in the heave direction, and E_{p2} is the power extracted from the pitching baffle. The conversion energy can be estimated using the following equations:

$$E_{p1} = \frac{B_{pto1}}{nT} \int_t^{t+nT} V^2 dt \tag{12}$$

$$E_{p2} = \frac{B_{pto2}}{nT} \int_t^{t+nT} \dot{\theta}^2 dt \tag{13}$$

where n is the number of the floater motion period, T is the wave period.

The incident wave power E_w can be calculated as:

$$E_w = \frac{1}{16} \frac{\rho g H_i^2 \omega D_y}{k} \left(1 + \frac{2kh}{sinh\ 2\ kh}\right) \tag{14}$$

where H_i is the incident wave height, h, k, ω are the water depth, wave number and wave frequency respectively, V is the heave velocity of the floater, and D_y is the transverse length of the floating breakwater.

- Wave transmission coefficient k_t.

The wave transmission coefficient k_t represents the functional role of a breakwater given the objective of wave protection, which is introduced as

$$k_t = \frac{H_t}{H_i} \tag{15}$$

where H_t is the transmission wave height obtained by a monitoring point set at x = 0.8 m behind the breakwater.

- Wave reflection coefficient K_r.

The wave reflection coefficient K_r is defined as the ratio of reflection wave height H_r to the incident wave height H_i, that is

$$K_r = \frac{H_r}{H_i} \tag{16}$$

where the reflection wave height H_r is calculated by the two-point method (Zhang et al., 2020a). To use this method, two monitoring points of wave elevation are set at $x_1 = -1.6$m and $x_2 = -2.4$m in front of the breakwater.

- Motion response ζ.

Table 1
Mesh grid and time step setups for the sensitivity study.

Parameters	Δx	Δz	Grid number	Time step	ΔT
Case A	0.01	0.01	150,686	0.003s	$T/533$
Case B	0.02	0.02	52,262	0.003s	$T/533$
Case C	0.005	0.005	442,526	0.003s	$T/533$
Case D	0.01	0.01	150,686	0.006s	$T/267$
Case E	0.01	0.01	150,686	0.0015s	$T/1066$

The motion response ζ is defined as the ratio of floater motion amplitude H_{system} to the incident wave height H_i.

$$\zeta = \frac{H_{system}}{H_i} \tag{17}$$

where the motion amplitude H_{system} is calculated using the Fast Fourier transform (FFT) method from the last five stable wave periods.

3. Verification and validation

3.1. Verification of numerical uncertainty

This section presents the verification procedure for the numerical uncertainty arising from grid densities and operating time steps. The FVM mesh is generated based on the regulation (ITTC and ITTC Quality System Manual Recommended Procedures and Guidelines, 2017), and the selection of time steps conforms to the Courant–Friedrichs–Lewy (CFL) condition. To carry out the mesh and time convergence studies, a representative case with a triangular-baffle geometry is used. Five cases (Case A, Case B, Case C, Case D, and Case E) are conducted with three different meshes and three different time steps, with the details summarized in Table 1.

Fig. 7 shows the numerical results, which include time-history wave velocity and structural heave motions under the wave condition $\omega = 3.97$ rad/s. Case A, with a coarse mesh, exhibits noticeable discrepancies at wave trough peaks, leading to reduced structure heave motion in Fig. 7(c). The medium time step of 0.003s ($T/533$) shows acceptable results in both wave generation and heave motions. However, case D with a time step of 0.006s may induce an error of about 6% on wave generation. Overall, Case B with mesh $\Delta z = H/12$ in the free surface region and time step $\Delta t = T/533$ provides sufficient accuracy for the considered applications, with the maximum attenuation of wave heights being less than 3.5%.

To ensure that numerical convergence is achieved for the CFD code, the uncertainty arising from grids and time steps is estimated based on the Grid Convergence Index (GCI) method (Stern et al., 2006). The numerical errors U_{SN} have three categories: iterative error U_I, grid size error U_G and time step error U_T The relation is expressed as: $U_{SN}{}^2 = U_I{}^2 + U_G{}^2 + U_T{}^2$. The iterative error raised by the normalized residuals when solving PDE equations, generally is negligible with at least three orders of magnitude decrease of error.

Grid and time convergence studies are performed using three solutions which are refined systematically with a refinement ratio. Define S_{k1}, S_{k2} and S_{k3} to be the solutions with fine, medium and coarse input parameters. The subscript k refers to the type of input parameters (i.e., G for grid size and T for time step). Differences between medium-fine $\varepsilon_{k21} = S_{k1} - S_{k2}$, and coarse-medium $\varepsilon_{k32} = S_{k3}$-$S_{k2}$ solutions are used to define the convergence ratio: $R_k = \frac{\varepsilon_{k21}}{\varepsilon_{k32}}$.

Three kinds of convergence can occur:

- $0 < R < 1$ Monolithic convergence (MC)
- $-1 < R < 0$ Oscillatory convergence (OC)
- $R > 1$ Monotonic divergence (MD)

The numerical error δ_k^* and order of accuracy P_k can be estimated by the generalised Richardson extrapolation

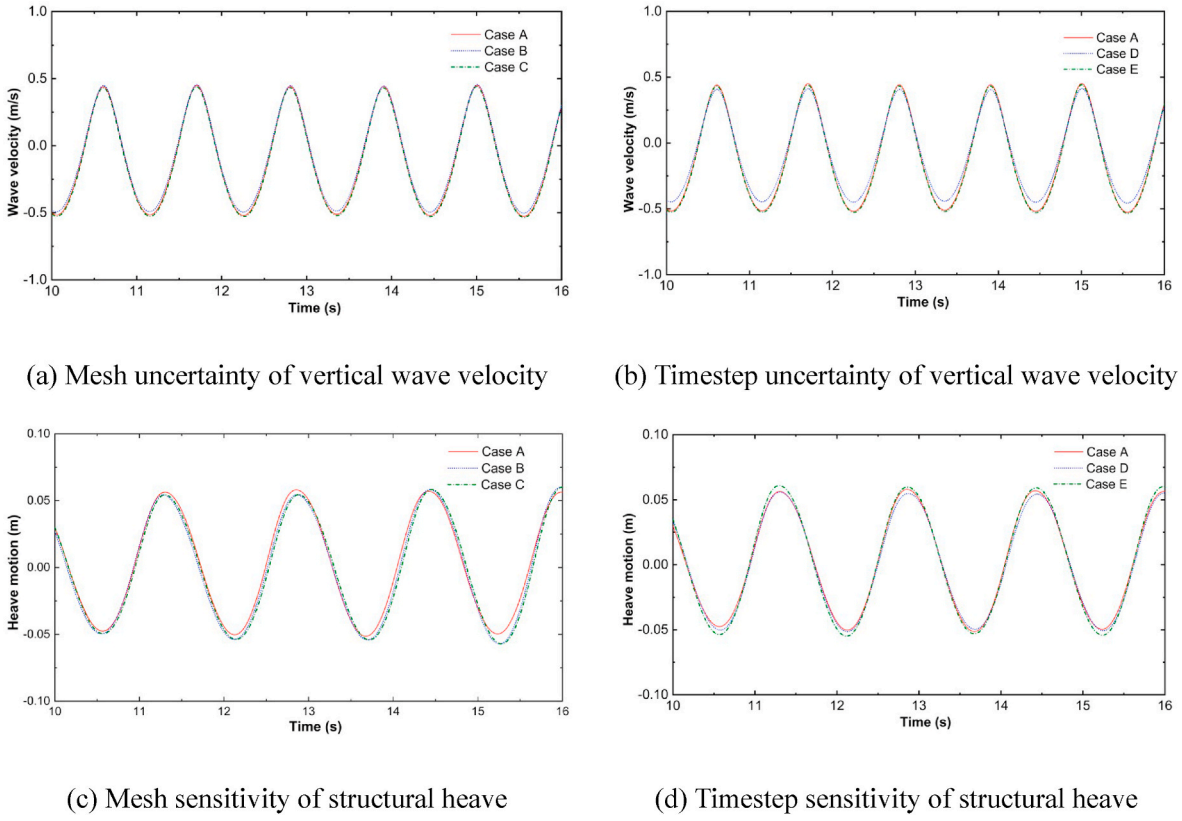

(a) Mesh uncertainty of vertical wave velocity

(b) Timestep uncertainty of vertical wave velocity

(c) Mesh sensitivity of structural heave

(d) Timestep sensitivity of structural heave

Fig. 7. Mesh and timestep sensitivity tests of a triangular-baffle bottom WEC of the hybrid system, with $H_i = 0.05\text{m}, \omega = 3.97$ rad/s.

Table 2
The GCI uncertainty analysis performed for the triangular-baffle case with wave condition $\omega = 3.97$ rad/s.

Mesh GCI	Max Vertical Wave Velocity (m/s)	ξ_s (m)	Timestep GCI	Max Vertical Wave Velocity (m/s)	ξ_s (m)
S_{G1}	0.0508	0.0533	S_{T1}	0.0509	0.0521
S_{G2}	0.0503	0.0515	S_{T2}	0.0503	0.0515
S_{G3}	0.0496	0.0505	S_{T3}	0.0492	0.0510
Refinement ratio r_{G21}	2.937	0.5	r_{T21}	2.937	0.5
Refinement ratio r_{G32}	2.883	0.5	r_{T32}	2.883	0.5
Convergence ratio R_G	0.24	0.3	R_G	0.667	0.45
Convergence type C_G	MC	MC	C_t	MC	MC
Order of accuracy P_G	0.60%	0.67%	P_T	0.64%	0.76%
Numerical error δ_G^*	1.75%	1.54%	δ_T^*	1.35%	2.139%
GCI uncertainty U_G	1.36%	1.23%	U_T	3.68%	2.44%

method:

$$\delta_k^* = \frac{\varepsilon_{k21}}{r_k^{p_k} - 1} \tag{18}$$

$$p_k = \frac{\ln\left(\varepsilon_{k21}/\varepsilon_{k32}\right)}{\ln\left(r_k\right)} \tag{19}$$

where, r_k is the refinement ratio between three solutions in grid and time step convergence studies. The GCI uncertainty U_k can then be estimated from numerical error δ_k^* multiplied by a factor of $F_s = 1.25$ to estimate the numerical error:

$$U_k = F_s * \left|\delta_k^*\right| \tag{20}$$

Table 2 shows that reasonably small levels of uncertainty are achieved for the wave velocity and heave responses in both time-step and mesh. However, a relatively large GCI uncertainty U_G is estimated in the time-step convergence study. This is mainly due to the selection of a coarse time step (T = 0.006s) that was too large for such an CFD simulation. Based on the considerations of the numerical accuracy and modelling effort, the medium mesh G_2 and medium time step T_2 are selected through all simulations.

3.2. Validation against experiments

In this paper, validation of the computational model is conducted on a pile-restrained floating square box in waves since there is no experimental results on the HH WEC-breakwater system. The simulation results are compared to the experimental results from (Ning et al., 2016), linear analytical method from (Zhao et al., 2017) and commercial CFD software from (Zhang et al., 2020a). The numerical model is demonstrated with the same scale ratio as it builds in the experimental model (Ning et al., 2016), the floating box has a length L_{xbox} of 0.8m, a height of L_{zbox} of 0.6m and the transverse length is calibrated as 0.01m due to the 2D modelling. The relative draft remains at $d/h = 0.2$ (draft $d = 0.2$m and water depth $h = 1$m) and the wave height $H_i/h = 0.12$ are considered. The PTO damping coefficient is set as 9.75 N/m. Fig. 8 shows four timesteps of a wave cycle on a representative case ($B/\lambda = 0.2, \omega = 4.02$Hz) of a free surface wave passing through the breakwater, with noticeable reflection and transmission.

Fig. 9 illustrates the variation of heave RAOs ξ_{RAO}, wave transmission coefficient K_t, conversional efficiency η_e and reflection coefficient K_r of the floating box against width ratio B/λ and wave frequency ω. The

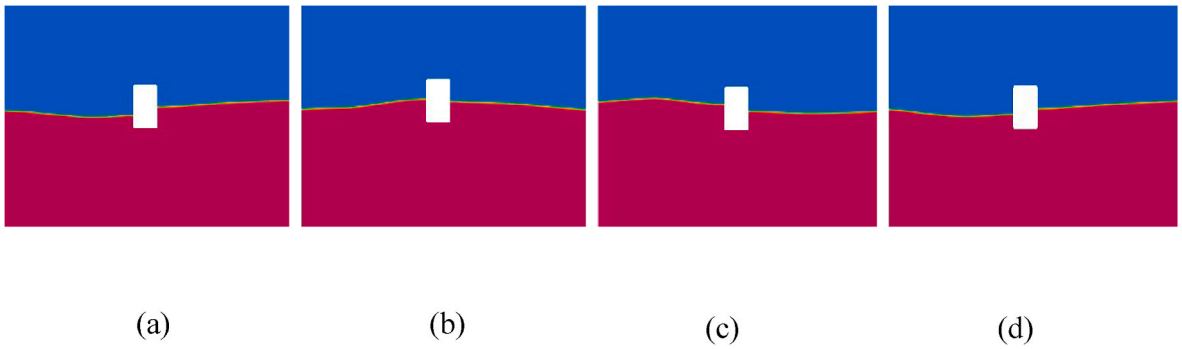

Fig. 8. Simulation example of the validation study for the box-shape WEC-breakwater system, (a) t = nT, (b) t = nT+1/4T, (c) t = nT+1/2T, (d) t = t = nT+1/2T.

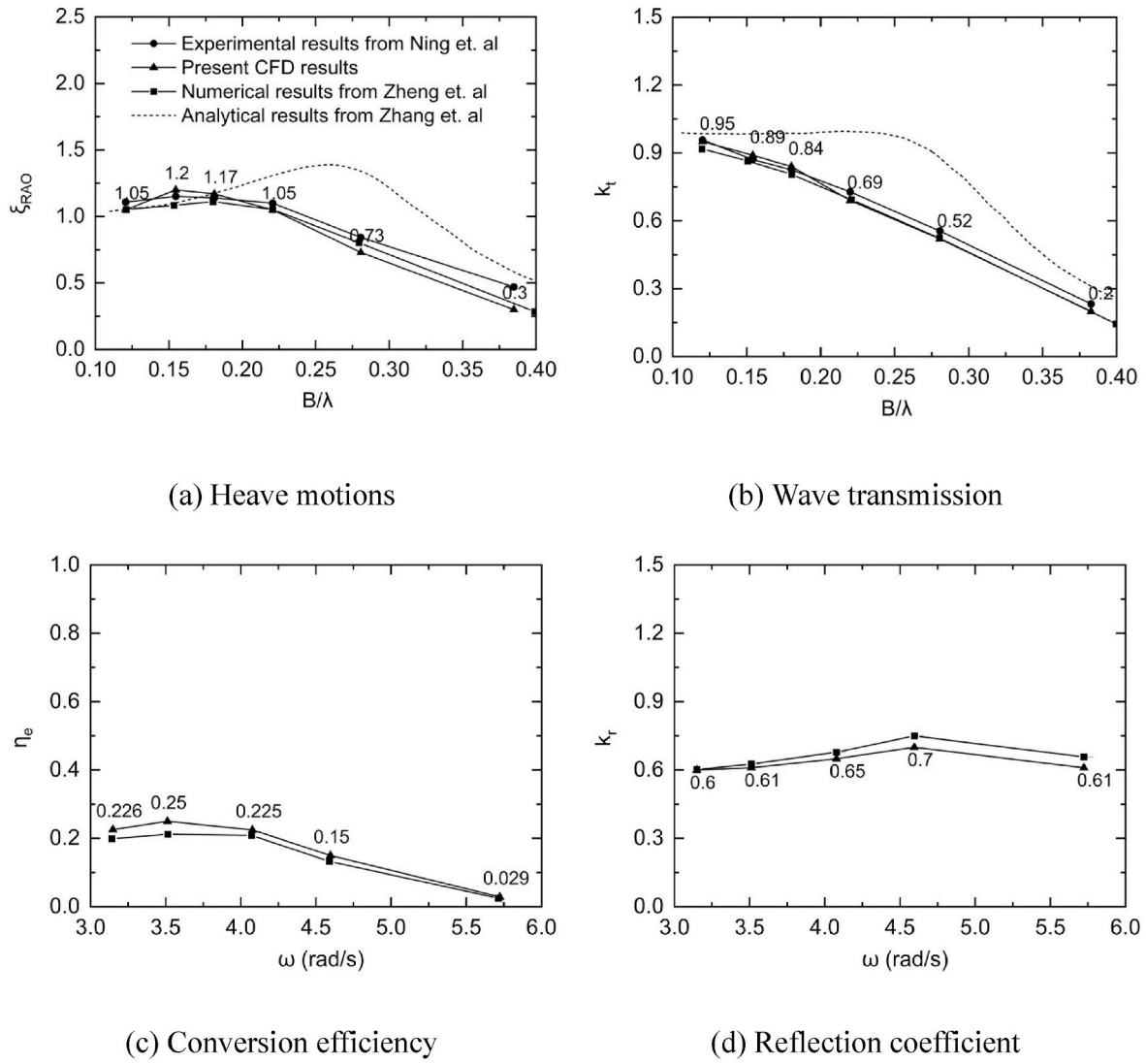

Fig. 9. Comparison of the hydrodynamic performance of different bottom shapes.

OpenFOAM results are represented using an upper triangular symbol and labelled. It can be seen that the heave motions ξ of the integrated system reached to the peak (about 1.2) at $B/\lambda = 0.15$, which represents the resonant frequency for the floating box. However, the maximum overestimation was about 9.5% and 14.6%, respectively, compared to the experimental work (Ning et al., 2016) and numerical results (Zhang et al., 2020a).

The wave transmission coefficient K_t decreases with an increase of B/λ, which implies the width of the breakwater has significant effects on its wave attenuation performance, as shown in Fig. 9(b). Compared to the linear potential numerical results (Zhao et al., 2017), it is observed that potential flow theory overpredicted the heave motions and wave transmission, as significant damping effects induced by viscous flow are not considered. Therefore, CFD studies are recommended for such

Table 3
Statistical comparison of the deviation between the present work and (Zhang et al., 2020a).

	Deviation					Mean
B/λ	**0.12**	**0.15**	**0.18**	**0.22**	**0.28**	
ξ_{RAO}	4.65%	6.55%	2.98%	3.44%	7.55%	5.03%
k_t	3.24%	1.96%	3.90%	1.15%	2.33%	2.52%
$\omega\ (rad/s)$	**3.15**	**3.51**	**4.08**	**4.59**	**5.72**	
η_e	11.77%	13.45%	5.98%	5.68%	2.56%	7.88%
k_r	2.25%	4.22%	5.42%	8.84%	9.45%	6.03%

studies.

The conversion efficiency η_e (Fig. 9(c)) and reflection coefficient K_r (Fig. 9(d)) of the present OpenFOAM results plot against wave frequency ω, show a similar trend to the StarCCM+ results (Zhang et al., 2020a). However, differences are noticeable in the reflection coefficient K_r at high wave frequencies for $\omega > 4.5$rad/s. This is closely related to the relaxation methods applied in the wave generation, which will affect the reflected wave propagation to the boundary. Therefore, it is recommended to place the relaxation zone far away from the structure. The deviation percentages between the present CFD simulation and (Zhang et al., 2020a) for key parameters are presented in Table 3. It is observed that the mean deviation across all parameters falls within the range of 2.5%–7.8%. This indicates that the overall agreement between the results obtained from the present CFD code and the literature is sufficiently low for all tested cases.

4. Results and discussion

Since the heave PTO and the hinge PTO have different optimal values in a wave condition, this section starts with both coefficients simultaneously and finds an optimal combination of them for the HH WEC-breakwater system. This is followed by an analysis of its hydrodynamic performance in waves, including dynamic motion, wave transmission, and energy conversion. The simulation results are compared with three contemporary shapes of WEC-breakwater systems, namely: square, wedge, and triangular baffle bottom.

4.1. Effect of mechanical damping

The hinge-baffle WEC-breakwater system consists of two bodies, connected with a spherical hinge. Two PTO systems are equipped: a heave direction damping system that resists the overall system in vertical velocity and a rotational damping that functions as a resisting torque proportional to the angular velocity of the baffle. Fig. 10 shows four timesteps of a wave cycle on a representative case ($\omega = 4.02$Hz) of a free surface wave passing through the HH type of WEC-breakwater system, with noticeable heave motions and hinge spinning.

The analytical method for calculating the natural frequency and optimal damping for a single WEC system is not suitable for the present case, as the two bodies' natural frequencies are not resonant harmonically. Therefore, two damping coefficients B_{PTO1} and B_{PTO2}, are required to be harmonised by finding their simultaneous optimal power output in varying wave conditions as shown in Fig. 11. It is seen that the dominant damping effect arises from at the resonant wave frequency ω close to 4.02 rad/s and the optimal damping coefficients are determined to be

Fig. 10. Simulation example of the HH WEC-breakwater system, (a) t = nT, (b) t = nT+1/4T, (c) t = nT+1/2T, (d) t = t = nT+1/2T.

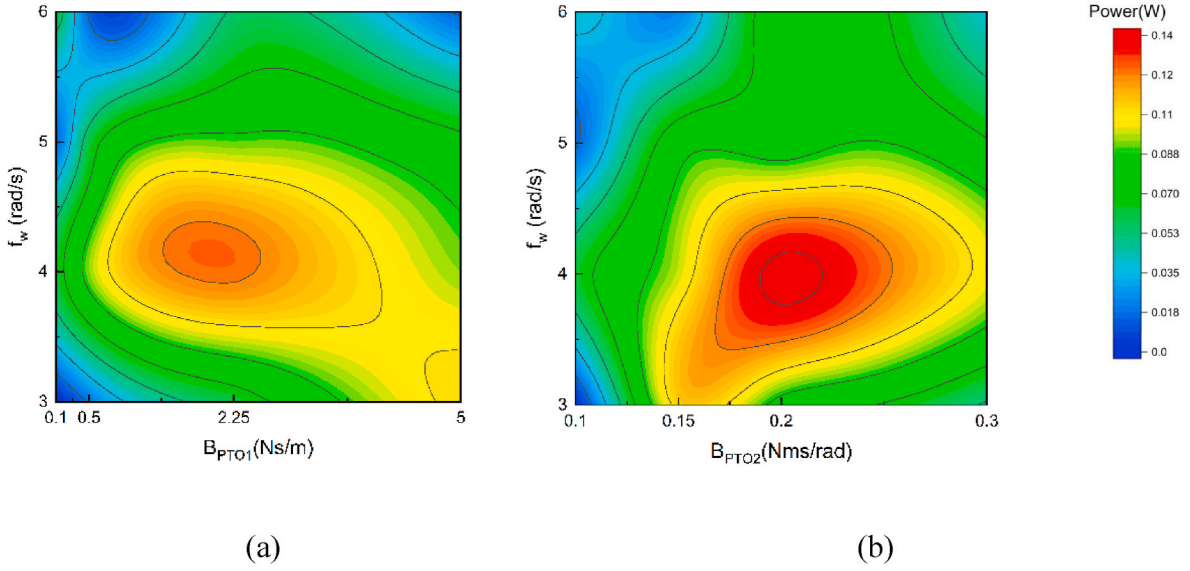

Fig. 11. Contour plots for the selection of optimal damping coefficients, (a) heave PTO, (b) hinge PTO.

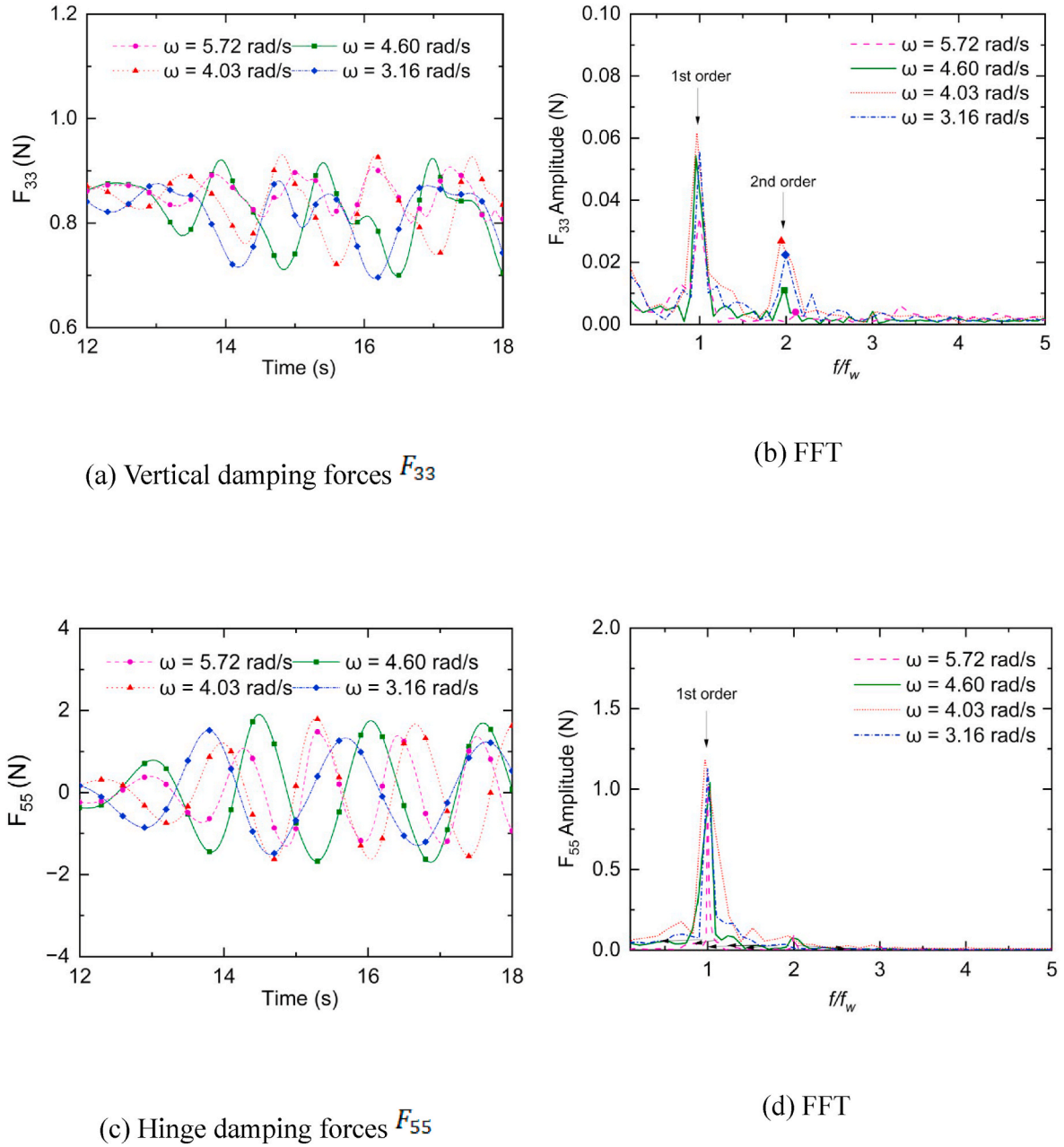

Fig. 12. Vertical and hinge damping forces for cases with optimal damping in waves.

$B_{PTO1} = 2.15Ns/m$ and $B_{PTO2} = 0.21Nms/rad$, representing the peak wave energy absorption. These findings indicate that the attachment of a hinged device introduces an additional resonance frequency, resulting in an extension of the capture width ratio. The integrated system can optimise its efficiency by properly adjusting the dual PTO damping.

Fig. 12 illustrates the damping forces on the heave PTO F_{33} and hinge rotational PTO F_{55} under varying wave conditions based on the optimal B_{pto} selections. Upon comparing the time-history results, high nonlinearity components are observed in F_{33}, with the largest peak occurring at the resonance wave conditions. An FFT analysis is conducted to obtain the frequency plot, which is presented in Fig. 12(b). The study finds that the main frequency of the signal coincides with the wave frequency, and the higher harmonic components in the forces are mainly due to the added hinged baffle.

Fig. 12(c) shows that the time-history hinge force F_{55} exhibits a general sinusoidal shape at different wave frequencies. Small peaks are noticed in the frequency analysis, which may arise from the nonlinearities in the wave-to-force process. Generally, the hinge damping force F_{55} is one order of magnitude (1:10) larger than the vertical damping force F_{33}. The difference between these two forces is due to the hinged baffle being excited by both horizontal and vertical wave particle velocities, while the global heave motion is mostly affected by the wave's vertical velocity.

Fig. 13 evaluates the vertical heave velocity $\dot{z}_3$ (drawn in black) and baffle angular velocity $\dot{\theta}_3$ (drawn in red) of the cases based on the optimal B_{PTO} under varying wave conditions. It is seen that $\dot{z}_3$ increases monotonically with increasing wave frequency ω. This is because the vertical oscillation of the system is dependent on the wave particle velocity, and longer waves have larger particle velocities. $\dot{\theta}_3$ is also influenced by the wave condition. It is interesting to note that the rotation speed reaches its maximum at the system wave resonance condition ($\omega = 4.02\,rad/s$). This indicates that the additional hinged spinning system has a minimal effect on the natural frequency of the

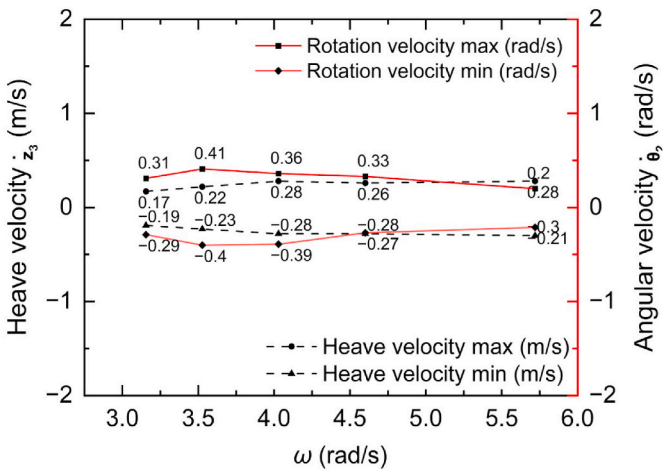

Fig. 13. The heave and angular velocity of the HH WEC-breakwater system in different wave frequencies, with optimized PTOs used.

entire system, although different sizes and materials of the added structure are not considered in this study. When the HH system is activated at its resonance frequency, it generally absorbs more energy than a single system without a hinge. As it is seen in Fig. 13, the magnitude of the $\dot{z}_3$ and the $\dot{\theta}_3$ are basically identical, but the hinge converted energy is less than the global vertical system due to B_{PTO2} being less than B_{PTO1}.

Fig. 14 shows the motion trajectory plots against time and space of the integrated breakwater-WEC with the optimal PTO selections in waves. It can be observed that the motion trajectory of the pitching baffle follows the same trend as that of the wave particles. Under short waves ($\omega > 4.60$rad/s), the baffle's motion trajectory takes on a flattened ellipse, where longitudinal motion is more dominant than lateral displacement, as shown in Fig. 14(b). The hinged baffle demonstrated a hysteresis phenomenon where the swing of baffle does not move symmetrically at the position of normalized $x = 0$, but instead tilts towards the wave propagation direction. This is due to the baffle not having fully restored to its original position, causing the wave force of the next wave to make it spin again. This phenomenon disappears under the cases in long waves (i.e. when $\omega = 3.16$ rad/s), as shown in Fig. 14(c and d), where the trajectory of the baffle is symmetrical along its initial position ($x = 0.75$m). This phenomenon could be related to the ratio between the wave period and the baffle's restoring period. When is greater than or equal to 1, the baffle's motion follows a closed elliptical trajectory, with one revolution aligning with the wave period. On the other hand, with short waves where is less than 1, the baffle's relatively large restoring period results in a delay and a phase difference between the wave and the baffle motions. This also comes with a smaller transmission coefficient for the short wave. These factors lead to irregularly shaped trajectories and non-overlapping periods, as shown in Fig. 14(b). In addition, the maximum power is observed at the resonant frequency ($\omega = 4.02$ rad/s), and the trajectory of the baffle presents a full ellipse form with a 0.019m horizontal displacement and a 0.125m vertical displacement.

4.2. Effect of floater shapes and connections

This section examines the effects of the bottom shape and connection methods on the motion characteristics and energy conversion performance of the integrated WEC-breakwater system in waves. Four bottom shapes are considered, square, wedge, triangular-baffle and hinged-baffle, as shown in Fig. 1. The width $B/h = 0.2$ and un-submerged height $D1/h = 0.2$ are kept the same throughout all cases. The mass of the integrated system is equal to the mass of the displacements of water at its initial draft, and the damping coefficient PTO is calibrated accordingly for optimization.

Fig. 15 displays the variation of heave motion ζ, heave velocity $\dot{z}_3$, transmission coefficient K_t and conversion efficiency η_e for four floater bottoms, as the wave frequency ranges from $3\,\text{rad/s} < \omega < 6\,\text{rad/s}$. It can be observed that the curves from ζ and K_t demonstrate similar trends regardless of the geometrical shapes. When comparing the square and wedge bottom shapes (same pre-defined draft ($D3/h = 0.16$)), the effect of asymmetrical bottom design on the body motion is significant. Especially, at $\omega = 3.60\,\text{rad/s}$, ζ reaches a maximum of 1.06 for the wedge bottom, while the square bottom only reaches 0.82. This is because waves passing through a wedge-shaped body induce large asymmetrical forces in the vertical direction, resulting in larger motions. The magnitude of K_t is dependent on wave conditions, indicating that the wave attenuation performance of such asymmetrical floaters is better for short waves.

The attachment of a baffle to the floater's bottom significantly impacts both ζ and K_t due to the increased draft of the body. The energy of the wave decreases with the water depth. Therefore, as the device draft increases, it will interact with more of the available wave energy and experience larger radiation damping. This leads to a higher conversion efficiency η_e for the floater with bottom attachments. Both baffle bottom cases have an increased range of motion amplitudes and relative velocity, resulting in more wave energy being extracted from them. Additionally, the magnitude of K_t is reduced by up to 60% for both baffle cases compared to the square and wedge bottom cases due to the added draft.

The K_t of HH system is slightly lower than that of the triangular baffle bottom when $3.5\,rad/s < \omega < 5\,rad/s$, implying that the hybrid system provides a reasonable improvement in wave attenuation for short waves. This is likely due to the rotation of the hinged baffle, which causes periodic changes in sub-merged body drafts. These changes affect the motion trajectory of water particles directly beneath the free surface, as depicted in Fig. 14(d). Additionally, the generation of vortices close to the oscillation structures further dissipates wave energy.

The conversion coefficient η_e is increased in the hinged-baffle case, as shown in Fig. 15(d), due to added rotation PTO B_{PTO2}. A general 5–11.5% increase in the magnitude of η_e can be observed through all wave frequencies for the hinged baffle case, as depicted in Fig. 15(d) when compared to the triangular baffle bottom. This finding points out that the HH breakwater-WEC system has the capability to extract energy along with the motion path in both heave and pitch directions, as seen in the motions shown in Fig. 15(a), boosting the energy conversion efficiency in comparison to the standalone WEC cases.

Fig. 16 presents a vorticity contour of the flow field with different bottom designs at various time instants during one wave cycle ($\omega = 3.14$rad/s). Fig. 16 (a) illustrates that two vortices are generated at the left and right corners symmetrically of the square bottom case in the wave cycle ($t, t + t/2$). Consequently, these eddies dissipate part of wave energy, associated with mass differences and inclination induced vertical components, finally resulting in less energy being extracted by the PTO from the square bottom floater.

The asymmetry attribute, i.e., the wedge bottom, with the same draft is shown in Fig. 16 (b). It is seen that the weaker vortices are generated close to the structure, leading to a larger conversion efficiency, as evidenced in Fig. 15 (d). Fig. 16(c) shows that due to the attachment of the bottom baffle, a strong vortex is formed at the bottom of the tip in region S1. The vortex may create a low-pressure area, leading to increased suction force at the tip. This, in turn, can increase the bending moment at the baffle corner, raising the probability of structural damage. Consequently, the development of stronger vortices near the bottom of the geometry can result in more energy being dissipated. In contrast, in the case of the hinged baffle shown in Fig. 16(d), the vortex is concentrated at the baffle tip due to the periodical baffle rotations. A pair of vortices is created at a certain distance from the baffle tips, and dissipated in water depth. This phenomenon occurs because the spinning baffle interacts with the wave passing through the bottom wedge, extracting energy from it. It is seen that the baffle dynamic motion alters

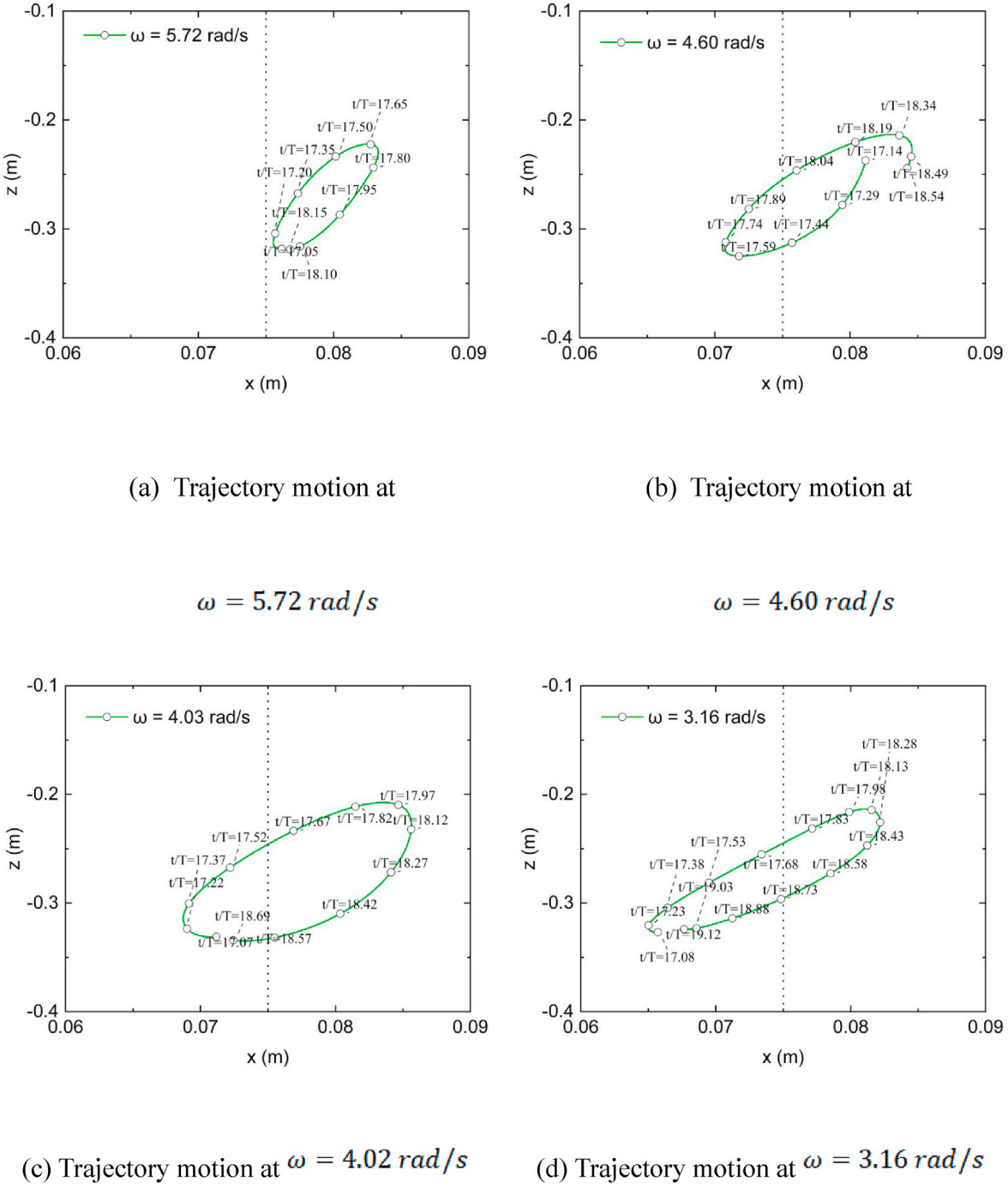

(a) Trajectory motion at $\omega = 5.72\ rad/s$

(b) Trajectory motion at $\omega = 4.60\ rad/s$

(c) Trajectory motion at $\omega = 4.02\ rad/s$

(d) Trajectory motion at $\omega = 3.16\ rad/s$

Fig. 14. Trajectory plots of the hinge device's centre of gravity.

the flow field beneath the floater's bottom and moves the vortex generation region further behind the geometry. As a result, this design solves the issues of structural stress concentration and energy loss found in traditional static breakwaters, ultimately aiming to improve the safety factor and service life of the structure.

5. Conclusions

This paper reported computational simulations on a heave-hinge WEC-breakwater system using a coupled FSI framework. Analysis was presented including the wave attenuation performance and energy conversion efficiency. Within the FSI framework, an open-source CFD toolbox, OpenFOAM was utilised as the fluid solver and MBDyn was selected as the multibody dynamic solver for solving structural parts. Data communication between two solvers was based on a fully two-way coupling algorithm. Two sets of energy conversion devices (heave damping PTO and rotational damping PTO) were equipped on the system to extract the wave energy at the air-water interface and beneath the free surface.

Before conducting systematic simulations, verification and validation were performed. The verification study first evaluated the effects of mesh grid and time step size on wave elevations and dynamic motions, using the GCI uncertainty approach. The validation study was carried out against an experiment of a box-shaped counterpart in regular waves (Ning et al., 2016). Linear analytical results (Zhao et al., 2017) and CFD results in literature (Zhang et al., 2020a) were also used to strengthen

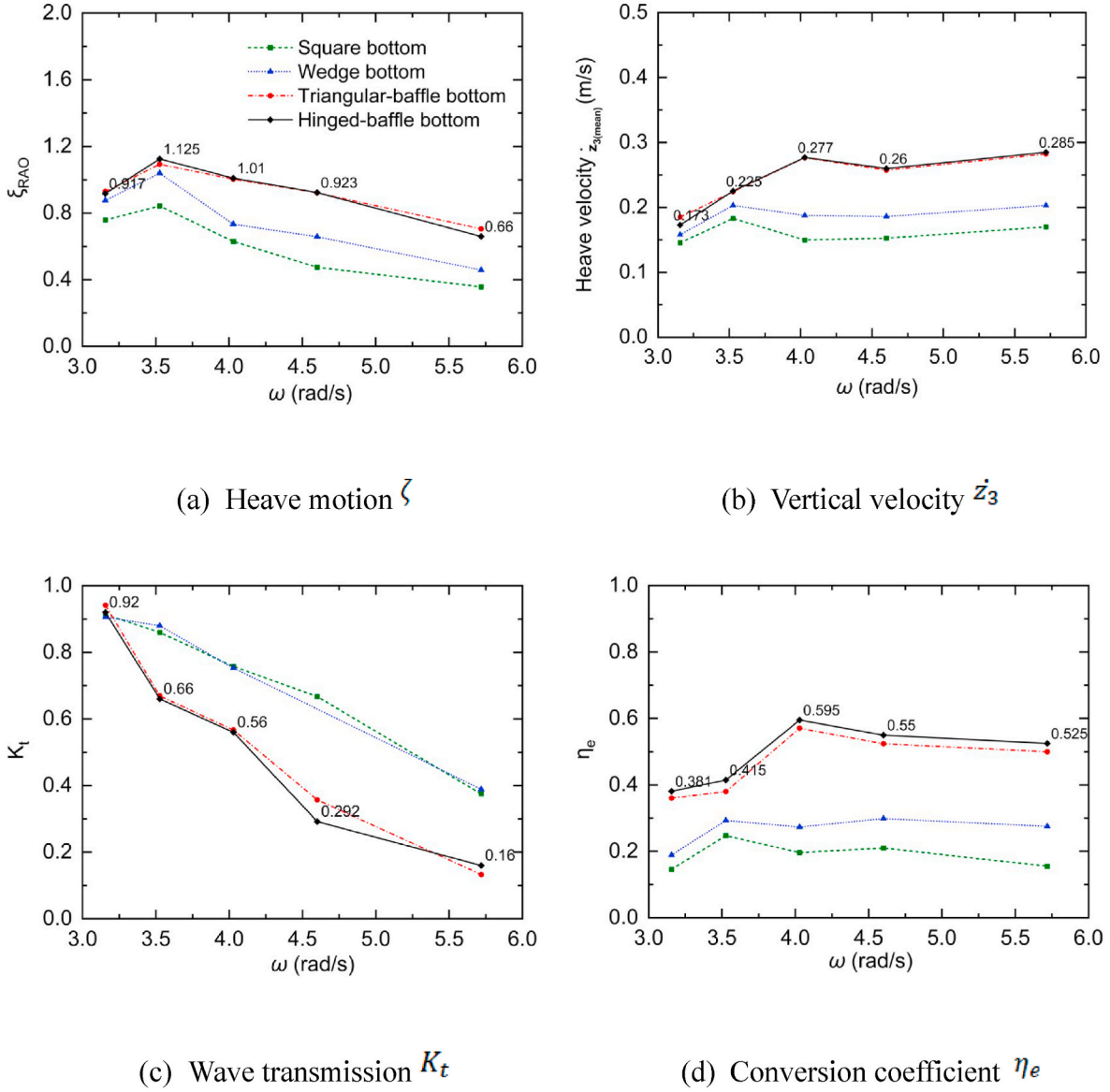

Fig. 15. Variation of ζ, $\dot{z}_3$, K_t and η_e versus ω for different bottom shapes under the optimal PTO damping.

the verification and validation process.

Subsequently, the performance of the heave-hinge type WEC-breakwater system was examined in various wave conditions. Due to the multi-body design of the system, the natural frequencies of each single body do not vibrate harmonically. Therefore, the dampings for both heave PTO and rotational PTO were optimized simultaneously. A series of analyses based on the optimal damping was then conducted, investigating damping forces, heave and angular velocities and motion trajectory of the baffle patches. In particular, the performance of the novel system was compared against three contemporary designs.

In-depth analysis has revealed that the shape of the bottom of the floater plays a significant factor in the hydrodynamic performance of the integrated system, as were the width and draft of the floaters. Among the various shapes analyzed, the square-bottomed floater is found to be the least suitable option. The energy efficiency and wave-damping performance of a square-bottomed floater are significantly lower compared to floaters with asymmetrical shapes. Therefore, it is advised to avoid using a floater with a square bottom in such applications.

The research also proposed a novel heave-hinge system by including a rotational PTO. When compared to a similar system without a hinge, the rotational PTO could potentially enhance the wave energy efficiency by as much as 11.5%. The improvement in dynamic motion and trajectory is primarily seen in shorter waves, where the system's natural frequency is related. In addition to the efficiency improvement, the vortex results obtained from the study have shown another crucial advantage of the attachment of hinged baffle.

Such concept design can reduce the aggregation of waves in front of the breakwater, resulting in the increase of converting unnecessary wave energy dissipation into an enhancement in the energy performance of the system. It also facilitates easy integration with existing infrastructures like solar farms or offshore platforms. The energy extracted from the hybrid system can be integrated into the existing energy grid to increase overall energy conversion, thereby reducing production and maintenance costs.

This paper selected regular waves as the research conditions and found out the optimal PTOs of the two parts separately for different regular wave conditions, and performed a hydrodynamic and energy assessment. In reality, there are irregular waves and a controlling system is expected to be used to adjust the system stiffness according to the dominating wave condition (based on the regular wave results), thus the system can operate in irregular waves with optimal performance. Future work is recommended to focus on studying the relevant stress

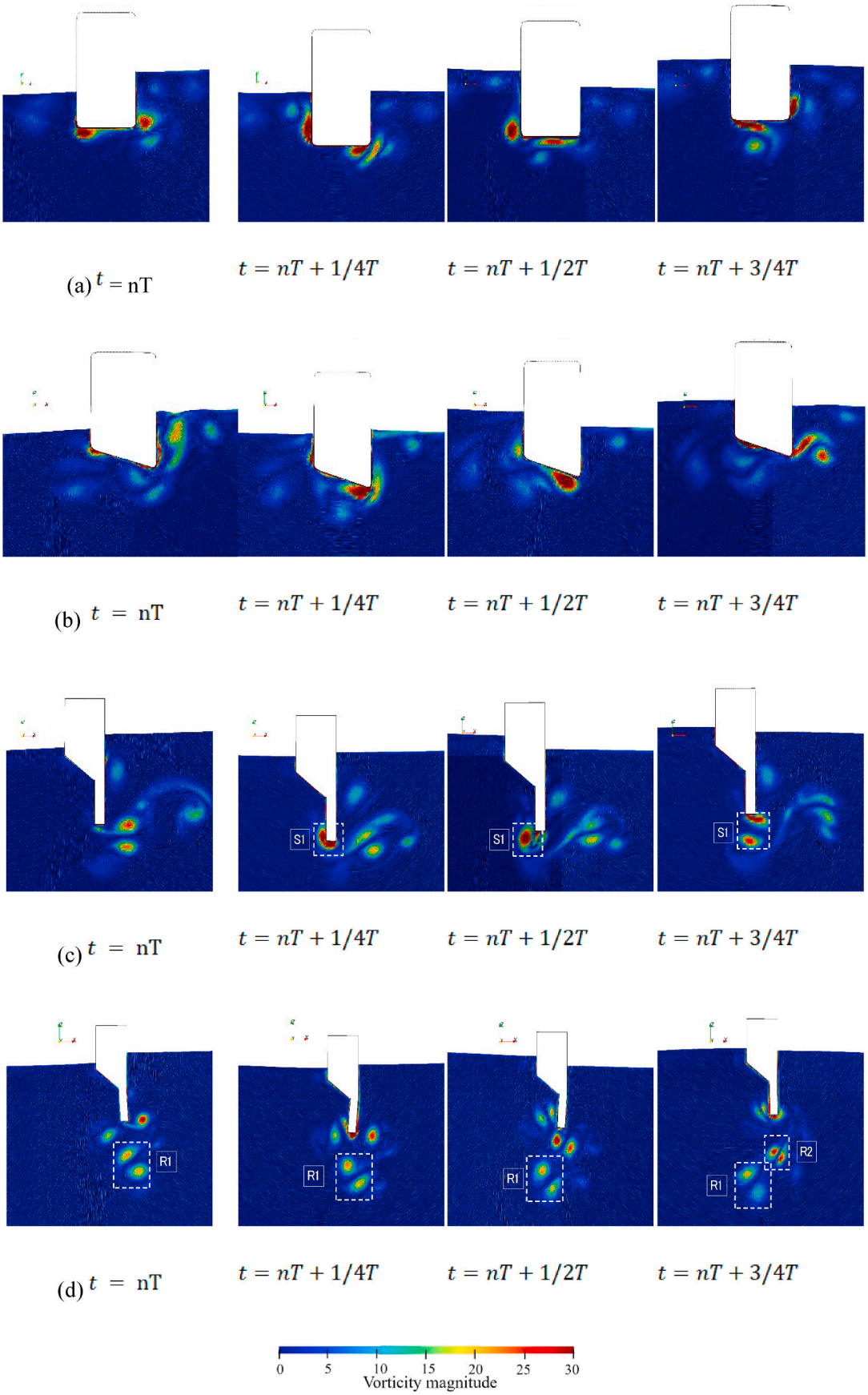

Fig. 16. Evolvement of the viscosity flow field with different WEC-breakwater geometries, (a) square bottom, (b) wedge bottom, (c) Triangular baffle bottom (d) Hinged baffle bottom.

concentration and fatigue performance of the hinged-heave WEC using Finite Element Analysis as this is highly related to the commercialisation of such systems.

CRediT authorship contribution statement

Yujia Wei: Conceptualization, Data curation, Formal analysis, Investigation, Methodology, Software, Validation, Visualization, Writing – original draft, Writing – review & editing. **Shuangrui Yu:** Formal analysis, Methodology, Writing – original draft, Conceptualization. **Xiang Li:** Formal analysis, Methodology, Writing – original draft, Conceptualization. **Chongwei Zhang:** Funding acquisition, Investigation, Resources, Supervision, Writing – review & editing, Methodology. **Dezhi Ning:** Funding acquisition, Resources, Supervision, Writing – review & editing. **Luofeng Huang:** Funding acquisition, Investigation, Methodology, Project administration, Resources, Supervision, Writing – original draft, Writing – review & editing.

Declaration of competing interest

The authors declare that they have no known competing financial interests or personal relationships that could have appeared to influence the work reported in this paper.

Data availability

All data underlying the results are available as part of the article and no additional source data are required.

Acknowledgements

L.H. acknowledges grants received from Innovate UK (No. 10048187, 10079774, 10081314) and the Royal Society (IEC\NSFC \223253, RG\R2\232462). The authors appreciate the High-Performance Computing system of Cranfield University, which was used to carry out the computational simulations.

Appendix A. Motion and PTO equations of the HH wave energy converter

This section presents an analytical derivation of the dynamic motion of the heave-hinge WEC-breakwater system. The integrated system consists of two separate PTO systems: the upper floater has a heave-direction PTO system, while the lower rotating baffle has a rotational PTO system along with the pitch direction. A spherical hinge confines three translational displacements of the rotating baffle, thereby only releasing the relative pitch motion. The dynamic motion of such a system can be expressed as follows:

$$\begin{bmatrix} M_{11}^1+m_{11}^1 & M_{13}^1+m_{13}^1 & \cdots & m_{11}^{12} & \cdots & \cdots \\ \cdots & M_{33}^1+m_{33}^1 & \cdots & \cdots & m_{33}^{12} & \cdots \\ \cdots & \cdots & M_{55}^1+m_{55}^1 & \cdots & \cdots & m_{55}^{12} \\ m_{11}^{21} & \cdots & \cdots & M_{11}^2+m_{11}^2 & \cdots & \cdots \\ \cdots & m_{33}^{21} & \cdots & \cdots & M_{33}^2+m_{33}^2 & \cdots \\ \cdots & \cdots & m_{33}^{21} & \cdots & \cdots & M_{55}^2+m_{55}^2 \end{bmatrix} \begin{bmatrix} \ddot{x}^1 \\ \ddot{z}^1 \\ \ddot{\theta}^1 \\ \ddot{x}^2 \\ \ddot{z}^2 \\ \ddot{\theta}^2 \end{bmatrix} + \begin{bmatrix} B_{11}^1 & \cdots & \cdots & B_{11}^{12} & \cdots & \cdots \\ \cdots & B_{33}^1+B_{\text{pto}}^1 & \cdots & \cdots & B_{33}^{12} & \cdots \\ \cdots & \cdots & B_{55}^1 & \cdots & \cdots & B_{55}^{12} \\ B_{11}^{21} & \cdots & \cdots & B_{11}^2 & \cdots & \cdots \\ \cdots & B_{33}^{21} & \cdots & \cdots & B_{33}^2 & \cdots \\ \cdots & \cdots & B_{33}^{21} & \cdots & \cdots & B_{55}^2+B_{\text{pto}}^2 \end{bmatrix} \begin{bmatrix} \dot{x}^1 \\ \dot{z}^1 \\ \dot{\theta}^1 \\ \dot{x}^2 \\ \dot{z}^2 \\ \dot{\theta}^2 \end{bmatrix}$$

$$+ \begin{bmatrix} K_{11}^1 & \cdots & \cdots & 0 & \cdots & \cdots \\ \cdots & K_{33}^1 & \cdots & \cdots & 0 & \cdots \\ \cdots & \cdots & K_{55}^1 & \cdots & \cdots & 0 \\ 0 & \cdots & \cdots & K_{11}^2 & \cdots & \cdots \\ \cdots & 0 & \cdots & \cdots & K_{33}^2 & \cdots \\ \cdots & \cdots & 0 & \cdots & \cdots & K_{55}^2 \end{bmatrix} \begin{bmatrix} x^1 \\ z^1 \\ \theta^1 \\ x^2 \\ z^2 \\ \theta^2 \end{bmatrix} = \begin{bmatrix} F_1^1+f_1^{12} \\ F_3^1+f_3^{12} \\ F_5^1+f_5^{12} \\ F_1^2+f_1^{21} \\ F_3^2+f_3^{21} \\ F_5^2+f_5^{21} \end{bmatrix} \tag{A1}$$

where, M and m are body mass and added mass separately, B is mechanical damping, and K is hydrostatic restoring stiffness, F denotes the external forces, z, $\dot{z}$ and $\ddot{z}$ are the heave displacement, velocity and acceleration of the system, correspondingly, θ, $\dot{\theta}$ and $\ddot{\theta}$ are the rotational angle, velocity and acceleration. The upper numbers mean body numbers, and the lower numbers denote the Degree Of Freedom (DOFs), $i = 1$–6 represents the DOF of a rigid body.

The spherical hinge is connected between the floater and the rotating baffle, thus there are only relative motions in the pitch directions at the hinge point. The hinge constrains the motions at the hinge point of the two bodies to be the same, except for the pitch direction. The relative rotational angle at the hinge point of the two hinged bodies can be calculated from the difference between their respective pitch angles in the body-fixed coordinate, therefore, the constraint equations are shown as follows.

$$\begin{bmatrix} M_{11}^1+m_{11}^1 & M_{13}^1+m_{13}^1 & \cdots & m_{11}^{12} & \cdots & \cdots \\ \cdots & M_{33}^1+m_{33}^1 & \cdots & \cdots & m_{33}^{12} & \cdots \\ \cdots & \cdots & M_{55}^1+m_{55}^1 & \cdots & \cdots & m_{55}^{12} \\ m_{11}^{21} & \cdots & \cdots & M_{11}^2+m_{11}^2 & \cdots & \cdots \\ \cdots & m_{33}^{21} & \cdots & \cdots & M_{33}^2+m_{33}^2 & \cdots \\ \cdots & \cdots & m_{33}^{21} & \cdots & \cdots & M_{55}^2+m_{55}^2 \end{bmatrix} \begin{bmatrix} 1 & 0 & 0 & 0 \\ 0 & 1 & 0 & 0 \\ 0 & 0 & 1 & 0 \\ 1 & 0 & R+r & -r \\ 0 & 1 & 0 & 0 \\ 0 & 0 & 1 & 1 \end{bmatrix} \begin{bmatrix} \ddot{x}^1 \\ \ddot{z}^1 \\ \ddot{\theta}^1 \\ \Delta\ddot{\theta}^{21} \end{bmatrix}$$

$$+ \begin{bmatrix} B_{11}^1 & \cdots & \cdots & B_{11}^{12} & \cdots & \cdots \\ \cdots & B_{33}^1+B_{\text{pto}}^1 & \cdots & \cdots & B_{33}^{12} & \cdots \\ \cdots & \cdots & B_{55}^1 & \cdots & \cdots & B_{55}^{12} \\ B_{11}^{21} & \cdots & \cdots & B_{11}^2 & \cdots & \cdots \\ \cdots & B_{33}^{21} & \cdots & \cdots & B_{33}^2 & \cdots \\ \cdots & \cdots & B_{33}^{21} & \cdots & \cdots & B_{55}^2+B_{\text{pto}}^2 \end{bmatrix} \begin{bmatrix} 1 & 0 & 0 & 0 \\ 0 & 1 & 0 & 0 \\ 0 & 0 & 1 & 0 \\ 1 & 0 & R+r & -r \\ 0 & 1 & 0 & 0 \\ 0 & 0 & 1 & 1 \end{bmatrix} \begin{bmatrix} \dot{x}^1 \\ \dot{z}^1 \\ \dot{\theta}^1 \\ \Delta\dot{\theta}^{21} \end{bmatrix} + \begin{bmatrix} K_{11}^1 & \cdots & \cdots & 0 & \cdots & \cdots \\ \cdots & K_{33}^1 & \cdots & \cdots & 0 & \cdots \\ \cdots & \cdots & K_{55}^1 & \cdots & \cdots & 0 \\ 0 & \cdots & \cdots & K_{11}^2 & \cdots & \cdots \\ \cdots & 0 & \cdots & \cdots & K_{33}^2 & \cdots \\ \cdots & \cdots & 0 & \cdots & \cdots & K_{55}^2 \end{bmatrix} \begin{bmatrix} 1 & 0 & 0 & 0 \\ 0 & 1 & 0 & 0 \\ 0 & 0 & 1 & 0 \\ 1 & 0 & R+r & -r \\ 0 & 1 & 0 & 0 \\ 0 & 0 & 1 & 1 \end{bmatrix} \begin{bmatrix} x^1 \\ z^1 \\ \theta^1 \\ \Delta\theta^{21} \end{bmatrix}$$

$$= \begin{bmatrix} F_1^1+f_1^{12} \\ F_3^1+f_3^{12} \\ F_5^1+f_5^{12} \\ F_1^2+f_1^{21} \\ F_3^2+f_3^{21} \\ F_5^2+f_5^{21} \end{bmatrix} \tag{A2}$$

multiply $\mathbf{S^T}$ at the two ends of the equation,

$$\boldsymbol{S}^{\mathbf{T}} \begin{bmatrix} M^1+m^1 & m^{12} \\ m^{21} & M^2+m^2 \end{bmatrix} \boldsymbol{S} \bullet \begin{bmatrix} \ddot{\boldsymbol{\eta}}^1 \\ \Delta\ddot{\theta}^{21} \end{bmatrix} + \boldsymbol{S}^{\mathbf{T}} \begin{bmatrix} B^1+B_{\text{pto}}^1 & B^{12} \\ B^{21} & B^2+B_{\text{pto}}^2 \end{bmatrix} \boldsymbol{S} \bullet \begin{bmatrix} \dot{\boldsymbol{\eta}}^1 \\ \Delta\dot{\theta}^{21} \end{bmatrix} + \boldsymbol{S}^{\mathbf{T}} \begin{bmatrix} K^1+K_{\text{pto}}^1 & 0 \\ 0 & K^2+K_{\text{pto}}^2 \end{bmatrix} \boldsymbol{S} \bullet \begin{bmatrix} \boldsymbol{\eta}^1 \\ \Delta\theta^{21} \end{bmatrix} = \boldsymbol{S}^{\mathbf{T}} \begin{bmatrix} F^1+f^{12} \\ F^2+f^{21} \end{bmatrix} \tag{A3}$$

where $\boldsymbol{I}$ is the identity matrix, S is the coefficient matrix of hinge constraints. R is the distance between the floater's CoG and the hinge point, r is the distance between the flap's CoG and the hinge point. Due to Newton's third law, the internal hinge forces can be eliminated. Therefore, the equations can be written as:

$$\boldsymbol{S}^{\mathbf{T}} \begin{bmatrix} f^{12} \\ f^{21} \end{bmatrix} = \begin{bmatrix} 1 & 0 & 0 & 1 & 0 & 0 \\ 0 & 1 & 0 & 0 & 1 & 0 \\ 0 & 0 & 1 & R+r & 0 & 1 \\ 0 & 0 & 0 & -r & 0 & 1 \end{bmatrix} \begin{bmatrix} f_1^{12} \\ f_3^{12} \\ f_5^{12} \\ f_1^{21} \\ f_3^{21} \\ f_5^{21} \end{bmatrix} = \begin{bmatrix} f_1^{12}+f_1^{21} \\ f_3^{12}+f_3^{21} \\ f_5^{12}+(R+r)f_1^{21}+f_5^{21} \\ -rf_1^{21}+f_5^{21} \end{bmatrix} = \begin{bmatrix} f_1^{12}-f_1^{12} \\ f_3^{12}-f_3^{12} \\ f_5^{12}+(R+r)f_1^{21}+f_5^{21} \\ -rf_1^{21}+f_5^{21} \end{bmatrix} = \mathbf{0} \tag{A4}$$

where, f denotes the internal hinge forces. So, the full form of equations can be written as:

$$
\begin{bmatrix} 1 & 0 & 0 & 1 & 0 & 0 \\ 0 & 1 & 0 & 0 & 1 & 0 \\ 0 & 0 & 1 & R+r & 0 & 1 \\ 0 & 0 & 0 & -r & 0 & 1 \end{bmatrix}
\begin{bmatrix} M_{11}^{1}+m_{11}^{1} & M_{13}^{1}+m_{13}^{1} & \cdots & m_{11}^{12} & \cdots & \cdots \\ \cdots & M_{33}^{1}+m_{33}^{1} & \cdots & \cdots & m_{33}^{12} & \cdots \\ \cdots & \cdots & M_{55}^{1}+m_{55}^{1} & \cdots & \cdots & m_{55}^{12} \\ m_{11}^{21} & \cdots & \cdots & M_{11}^{2}+m_{11}^{2} & \cdots & \cdots \\ \cdots & m_{33}^{21} & \cdots & \cdots & M_{33}^{2}+m_{33}^{2} & \cdots \\ \cdots & \cdots & m_{33}^{21} & \cdots & \cdots & M_{55}^{2}+m_{55}^{2} \end{bmatrix}
\begin{bmatrix} 1 & 0 & 0 & 0 \\ 0 & 1 & 0 & 0 \\ 0 & 0 & 1 & 0 \\ 1 & 0 & R+r & -r \\ 0 & 1 & 0 & 0 \\ 0 & 0 & 1 & 1 \end{bmatrix}
\begin{bmatrix} \ddot{x}^{1} \\ \ddot{z}^{1} \\ \ddot{\theta}^{1} \\ \Delta\ddot{\theta}^{21} \end{bmatrix}
$$

$$
+ \begin{bmatrix} 1 & 0 & 0 & 1 & 0 & 0 \\ 0 & 1 & 0 & 0 & 1 & 0 \\ 0 & 0 & 1 & R+r & 0 & 1 \\ 0 & 0 & 0 & -r & 0 & 1 \end{bmatrix}
\begin{bmatrix} B_{11}^{1} & \cdots & \cdots & B_{11}^{12} & \cdots & \cdots \\ \cdots & B_{33}^{1}+B_{\mathrm{pto}}^{1} & \cdots & \cdots & B_{33}^{12} & \cdots \\ \cdots & \cdots & B_{55}^{1} & \cdots & \cdots & B_{55}^{12} \\ B_{11}^{21} & \cdots & \cdots & B_{11}^{2} & \cdots & \cdots \\ \cdots & B_{33}^{21} & \cdots & \cdots & B_{33}^{2} & \cdots \\ \cdots & \cdots & B_{33}^{21} & \cdots & \cdots & B_{55}^{2}+B_{\mathrm{pto}}^{2} \end{bmatrix}
\begin{bmatrix} 1 & 0 & 0 & 0 \\ 0 & 1 & 0 & 0 \\ 0 & 0 & 1 & 0 \\ 1 & 0 & R+r & -r \\ 0 & 1 & 0 & 0 \\ 0 & 0 & 1 & 1 \end{bmatrix}
\begin{bmatrix} \dot{x}^{1} \\ \dot{z}^{1} \\ \dot{\theta}^{1} \\ \Delta\dot{\theta}^{21} \end{bmatrix}
$$

$$
+ \begin{bmatrix} 1 & 0 & 0 & 1 & 0 & 0 \\ 0 & 1 & 0 & 0 & 1 & 0 \\ 0 & 0 & 1 & R+r & 0 & 1 \\ 0 & 0 & 0 & -r & 0 & 1 \end{bmatrix}
\begin{bmatrix} K_{11}^{1} & \cdots & \cdots & 0 & \cdots & \cdots \\ \cdots & K_{33}^{1} & \cdots & \cdots & 0 & \cdots \\ \cdots & \cdots & K_{55}^{1} & \cdots & \cdots & 0 \\ 0 & \cdots & \cdots & K_{11}^{2} & \cdots & \cdots \\ \cdots & 0 & \cdots & \cdots & K_{33}^{2} & \cdots \\ \cdots & \cdots & 0 & \cdots & \cdots & K_{55}^{2} \end{bmatrix}
\begin{bmatrix} 1 & 0 & 0 & 0 \\ 0 & 1 & 0 & 0 \\ 0 & 0 & 1 & 0 \\ 1 & 0 & R+r & -r \\ 0 & 1 & 0 & 0 \\ 0 & 0 & 1 & 1 \end{bmatrix}
\begin{bmatrix} x^{1} \\ z^{1} \\ \theta^{1} \\ \Delta\theta^{21} \end{bmatrix}
= \begin{bmatrix} F_{1}^{1} \\ F_{3}^{1} \\ F_{5}^{1} \\ F_{1}^{2} \\ F_{3}^{2} \\ F_{5}^{2} \end{bmatrix}
\tag{A5}
$$

References

Adee, B.H.A., 1976. Review of developments and problems in using floating breakwaters. In: Offshore Technology Conference. OnePetro.

Benites-Munoz, D., Huang, L., Anderlini, E., Marín-Lopez, J.R., Thomas, G., 2020. Hydrodynamic modelling of an oscillating wave surge converter including power take-off. J. Mar. Sci. Eng. 8 (10), 771.

Bozzi, S., Miquel, A., Antonini, A., Passoni, G., Archetti, R., 2013. Modeling of a point absorber for energy conversion in Italian Seas. Energies 6 (6), 3033–3051.

Chen, Y.-k., Liu, Y., Meringolo, D.D., Hu, J.-m., 2023. Study on the hydrodynamics of a twin floating breakwater by using SPH method. Coast. Eng. 179, 104230.

Cheng, Y., Du, W., Dai, S., Ji, C., Collu, M., Cocard, M., Cui, L., Yuan, Z., Incecik, A., 2022a. Hydrodynamic Characteristics of a Hybrid Oscillating Water Column-Oscillating Buoy Wave Energy Converter Integrated into a π-type Floating Breakwater. Renewable and Sustainable Energy Reviews, p. 161.

Cheng, Y., Fu, L., Dai, S., Collu, M., Cui, L., Yuan, Z., Incecik, A., 2022b. Experimental and numerical analysis of a hybrid WEC-breakwater system combining an oscillating water column and an oscillating buoy. Renew. Sustain. Energy Rev. 169, 112909.

Cheng, Y., Fu, L., Dai, S., Collu, M., Ji, C., Yuan, Z., Incecik, A., 2022c. Experimental and numerical investigation of WEC-type floating breakwaters: a single-pontoon oscillating buoy and a dual-pontoon oscillating water column. Coast. Eng. 177, 104188.

Dai, J., Wang, C.M., Utsunomiya, T., Duan, W., 2018. Review of recent research and developments on floating breakwaters. Ocean Eng. 158, 132–151.

Diamantoulaki, I., Angelides, D.C., Manolis, G.D., 2008. Performance of pile-restrained flexible floating breakwaters. Appl. Ocean Res. 30 (4), 243–255.

Elhanafi, A., Macfarlane, G., Fleming, A., Leong, Z., 2017. Experimental and numerical investigations on the hydrodynamic performance of a floating–moored oscillating water column wave energy converter. Appl. Energy 205, 369–390.

Guo, B., Ning, D., Wang, R., Ding, B., 2021. Hydrodynamics of an oscillating water column WEC - breakwater integrated system with a pitching front-wall. Renew. Energy 176, 67–80.

He, F., Huang, Z., 2014. Hydrodynamic performance of pile-supported OWC-type structures as breakwaters: an experimental study. Ocean Eng. 88, 618–626.

Hirt, C.W., Nichols, B.D., 1981. Volume of fluid (VOF) method for the dynamics of free boundaries. J. Comput. Phys. 39 (1), 201–225.

Huang, L., Li, Y., 2022a. Design of the submerged horizontal plate breakwater using a fully coupled hydroelastic approach. Comput. Aided Civ. Infrastruct. Eng. 37 (7), 915–932.

Huang, L., Li, Y., Benites-Munoz, D., Windt, C.W., Feichtner, A., Tavakoli, S., Davidson, J., Paredes, R., Quintuna, T., Ransley, E., 2022b. A review on the modelling of wave-structure interactions based on OpenFOAM. OpenFOAM® Journal 2, 116–142.

ITTC, ITTC Quality System Manual Recommended Procedures and Guidelines, 2017. Seakeeping Committe of the 28th ITTC.

Jacobsen, N.G., Fuhrman, D.R., Fredsøe, J., 2012. A wave generation toolbox for the open-source CFD library: OpenFoam®. Int. J. Numer. Methods Fluid. 70 (9), 1073–1088.

Jasak, J.H.A., Tukovic, Z., 2007. OpenFOAM: a C++ library for complex physics simulations. International Workshop on Coupled Methods in Numerical Dynamics 1000, 1–20.

Khojasteh, D., Shamsipour, A., Huang, L., Tavakoli, S., Haghani, M., Flocard, F., Farzadkhoo, M., Iglesias, G., Hemer, M., Lewis, M., 2023. A large-scale review of wave and tidal energy research over the last 20 years. Ocean Eng. 282, 114995.

Koutandos, E., Karambas, T.V., Koutitas, C., 2004. Floating breakwater response to waves action using a Boussinesq model coupled with a 2DV elliptic solver. J. Waterw. Port, Coast. Ocean Eng. 130 (5), 243–255.

Luo, Y., Wang, Z., Peng, G., Xiao, Y., Zhai, L., Liu, X., Zhang, Q., 2014. Numerical simulation of a heave-only floating OWC (oscillating water column) device. Energy 76, 799–806.

Madhi, F., Sinclair, M.E., Yeung, R.W., 2014. The "Berkeley Wedge": an asymmetrical energy-capturing floating breakwater of high performance*. Marine systems & ocean technology 9, 5–16.

Maritime, Journal, 2005. Breakwater Beats the Weather at Holy Loch.

Méhauté, B., 1976. In: Media, S.S.B. (Ed.), An Introduction to Hydrodynamics and Water Waves.

Ning, D., Zhao, X., Göteman, M., Kang, H., 2016. Hydrodynamic performance of a pile-restrained WEC-type floating breakwater: an experimental study. Renew. Energy 95, 531–541.

Ning, D.-Z., Zhao, X.-L., Zhao, M., Hann, M., Kang, H.-G., 2017. Analytical investigation of hydrodynamic performance of a dual pontoon WEC-type breakwater. Appl. Ocean Res. 65, 102–111.

Ram, G., Saad, M.R., Zainal Abidin, N., Abdul Rahman, M.R., 2022. Hydrodynamic performance of a hybrid system of a floating oscillating water column and a breakwater. Ocean Eng. 264.

Reabroy, R., Zheng, X., Zhang, L., Zang, J., Yuan, Z., Liu, M., Sun, K., Tiaple, Y., 2019. Hydrodynamic response and power efficiency analysis of heaving wave energy converter integrated with breakwater. Energy Convers. Manag. 195, 1174–1186.

Stern, F., Wilson, R., Shao, J., 2006. Quantitative V&V of CFD simulations and certification of CFD codes. Int. J. Numer. Methods Fluid. 50 (11), 1335–1355.

Tagliafierro, B., Martínez-Estévez, I., Domínguez, J.M., Crespo, A.J., Göteman, M., Engström, J., Gómez-Gesteira, M., 2022. A numerical study of a taut-moored point-

absorber wave energy converter with a linear power take-off system under extreme wave conditions. Appl. Energy 311, 118629.
Vicente, P.C., Falcão, A.F.O., Justino, P.A.P., 2013. Nonlinear dynamics of a tightly moored point-absorber wave energy converter. Ocean Eng. 59, 20–36.
Wei, A. Incecik, Tezdogan, T., 2022. A fully coupled CFD-DMB approach on the ship hydroelasticity of a containership in extreme wave conditions. J. Mar. Sci. Eng. 10 (11), 1778.
Wei, Y., Wang, J., Yang, L., Luo, J., Jain, S., Hetharia, W., Riyadi, S., Utama, I., Huang, L., 2023. Simulation of a floating solar farm in waves with a novel suntracking system. In: Proceedings of the 12th International Workshop on Ship and Marine Hydrodynamics. Espoo, Finland.
Xu, Q., Li, Y., Yu, Y.-H., Ding, B., Jiang, Z., Lin, Z., Cazzolato, B., 2019. Experimental and numerical investigations of a two-body floating-point absorber wave energy converter in regular waves. J. Fluid Struct. 91.
Yu, H.-F., Zhang, Y.-L., Zheng, S.-M., 2016. Numerical study on the performance of a wave energy converter with three hinged bodies. Renew. Energy 99, 1276–1286.
Yu, S., Zhang, M., Chen, M., Chen, M., Yuan, Z., 2023. Pitch motion control of spar-type floating wind turbines. In: Proceedings of the ASME 2023 42nd International Conference on Ocean, Offshore and Arctic Engineering OMAE2023. Melbourne, Australia.
Zhang, H., Zhou, B., Vogel, C., Willden, R., Zang, J., Zhang, L., 2020a. Hydrodynamic Performance of a Floating Breakwater as an Oscillating-Buoy Type Wave Energy Converter. Applied Energy, p. 257.
Zhang, H., Zhou, B., Vogel, C., Willden, R., Zang, J., Geng, J., 2020b. Hydrodynamic performance of a dual-floater hybrid system combining a floating breakwater and an oscillating-buoy type wave energy converter. Appl. Energy 259.
Zhang, Y., Li, M., Zhao, X., Chen, L., 2020c. The effect of the coastal reflection on the performance of a floating breakwater-WEC system. Appl. Ocean Res. 100.
Zhao, X., Ning, D., Zhang, C., Kang, H., 2017. Hydrodynamic investigation of an oscillating buoy wave energy converter integrated into a pile-restrained floating breakwater. Energies 10 (5).
Zhao, X., Ning, D., 2018. Experimental investigation of breakwater-type WEC composed of both stationary and floating pontoons. Energy 155, 226–233.
Zhao, X.L., Ning, D.Z., Zou, Q.P., Qiao, D.S., Cai, S.Q., 2019. Hybrid floating breakwater-WEC system: a review. Ocean Eng. 186.
Zhao, X., Xue, R., Geng, J., Göteman, M., 2021. Analytical investigation on the hydrodynamic performance of a multi-pontoon breakwater-WEC system. Ocean Eng. 220.
Zhou, B., Zheng, Z., Jin, P., Wang, L., Zang, J., 2022. Wave attenuation and focusing performance of parallel twin parabolic arc floating breakwaters. Energy 260, 125164.